https://doi.org/10.3847/1538-3881/ac9c5c

CrossMark

Systematic KMTNet Planetary Anomaly Search. VI. Complete Sample of 2018 Sub-prime-field Planets

Youn Kil Jung[1,2], Weicheng Zang[3], Cheongho Han[4], Andrew Gould[5,6], Andrzej Udalski[7]
(Lead Authors),

Michael D. Albrow[8], Sun-Ju Chung[1], Kyu-Ha Hwang[1], Yoon-Hyun Ryu[1], In-Gu Shin[4], Yossi Shvartzvald[9], Hongjing Yang[3], Jennifer C. Yee[10], Sang-Mok Cha[11], Dong-Jin Kim[1], Seung-Lee Kim[1], Chung-Uk Lee[1], Dong-Joo Lee[1], Yongseok Lee[1,11], Byeong-Gon Park[1,2], Richard W. Pogge[6]
(The KMTNet Collaboration),
and
Przemek Mróz[7], Michał K. Szymański[7], Jan Skowron[7], Radek Poleski[7], Igor Soszyński[7], Paweł Pietrukowicz[7], Szymon Kozłowski[7], Krzysztof Ulaczyk[12], Krzysztof A. Rybicki[7,9], Patryk Iwanek[7], and Marcin Wrona[7]
(The OGLE Collaboration)

[1] Korea Astronomy and Space Science Institute, Daejon 34055, Republic of Korea; younkil21@gmail.com
[2] Korea University of Science and Technology, Korea, (UST), 217 Gajeong-ro, Yuseong-gu, Daejeon, 34113, Republic of Korea
[3] Department of Astronomy, Tsinghua University, Beijing 100084, People's Republic of China
[4] Department of Physics, Chungbuk National University, Cheongju 28644, Republic of Korea
[5] Max-Planck-Institute for Astronomy, Königstuhl 17, D-69117 Heidelberg, Germany
[6] Department of Astronomy, Ohio State University, 140 W. 18th Avenue, Columbus, OH 43210, USA
[7] Astronomical Observatory, University of Warsaw, Al. Ujazdowskie 4, 00-478 Warszawa, Poland
[8] University of Canterbury, Department of Physics and Astronomy, Private Bag 4800, Christchurch 8020, New Zealand
[9] Department of Particle Physics and Astrophysics, Weizmann Institute of Science, Rehovot 76100, Israel
[10] Center for Astrophysics | Harvard & Smithsonian, 60 Garden Street, Cambridge, MA 02138, USA
[11] School of Space Research, Kyung Hee University, Yongin, Kyeonggi 17104, Republic of Korea
[12] Department of Physics, University of Warwick, Gibbet Hill Road, Coventry, CV4 7AL, UK

Abstract

We complete the analysis of all 2018 sub-prime-field microlensing planets identified by the KMTNet AnomalyFinder. Among the 9 previously unpublished events with clear planetary solutions, 6 are clearly planetary (OGLE-2018-BLG-0298, KMT-2018-BLG-0087, KMT-2018-BLG-0247, KMT-2018-BLG-0030, OGLE-2018-BLG-1119, and KMT-2018-BLG-2602), while the remaining 3 are ambiguous in nature. The above ordering of these events is made to facilitate grouping of their Bayesian estimates: the first two are lower-mass gas giants while the last four are Jovian-class planets; the first three most likely lie in the bulge, the last in the disk, and the remaining two are equally likely to be in either population. More specifically, these six planets have host masses $M_{\rm host} = (0.69^{+0.34}_{-0.30}, 0.10^{+0.14}_{-0.05}, 0.29^{+0.28}_{-0.14}, 0.51^{+0.43}_{-0.31}, 0.48^{+0.35}_{-0.28}, 0.66^{+0.42}_{-0.36})M_\odot$, planet masses $M_{\rm planet} = (0.14^{+0.07}_{-0.06}, 0.23^{+0.32}_{-0.12}, 2.11^{+2.09}_{-1.04}, 1.45^{+1.23}_{-0.88}, 0.91^{+0.66}_{-0.52}, 1.15^{+0.73}_{-0.63})M_{\rm Jup}$, and distances $D_L = (6.54^{+0.95}_{-1.23}, 7.02^{+1.03}_{-1.15}, 6.76^{+0.99}_{-1.24}, 6.48^{+1.28}_{-1.96}, 5.76^{+1.43}_{-2.48}, 4.31^{+1.97}_{-1.84})$kpc. In addition, there are 8 previously published sub-prime-field planets that were selected by the AnomalyFinder algorithm. Together with a companion paper on 2018 prime-field planets, this work lays the basis for comprehensive statistical studies. We carry out two such studies, one on caustic topologies and the other on the role of Gaia data. From the first, as expected, half (17/33) of the 2018 planets likely to enter the mass-ratio analysis have non-caustic-crossing anomalies. However, only 1 of the 5 noncaustic anomalies with planet-host mass ratio $q < 10^{-3}$ was discovered by eye (compared to 7 of the 12 with $q > 10^{-3}$), showing the importance of the semiautomated AnomalyFinder search. From the second, we find that Gaia has played a major role in the interpretation of 16% of the sample and a supplementary role in 6%.

1. Introduction

This paper completes the publication of all planetary events that were identified by the KMTNet AnomalyFinder algorithm (Zang et al. 2021, 2022b) that occurred during the 2018 season within the 21 subprime KMTNet fields. It is a companion to a paper on the 2018 prime-field planets by Gould et al. (2022), which analyzed 10 new planetary (or potentially planetary) events, and summarized 4 previous AnomalyFinder 2018 prime-field discoveries (Wang et al. 2022; Hwang et al. 2022), as well as 12 previously analyzed planetary (or possibly planetary) events that were recovered by AnomalyFinder. These 26 events are listed in their Table 11. The above references are, respectively, Papers I, IV, II, III, and V, in the AnomalyFinder series. The locations and cadences of the KMTNet fields are shown in Figure 12 of Kim et al. (2018a).

Table 1
Event Names, Cadences, Alerts, and Locations

Name	Γ (hr^{-1})	Alert Date	R.A.$_{\rm J2000}$	Decl.$_{\rm J2000}$	l	b
KMT-2018-BLG-0030	1.0	21 Jun 2018	17:38:04.00	−28:02:29.85	−0.11	+1.88
KMT-2018-BLG-0087	2.0	21 Jun 2018	17:37:18.48	−27:49:55.42	−0.03	+2.14
KMT-2018-BLG-0247	1.0	08 Jul 2018	17:38:14.41	−27:09:01.48	+0.66	+2.33
OGLE-2018-BLG-1219	1.3					
OGLE-2018-BLG-0298	1.0	05 Mar 2018	17:37:08.28	−29:42:32.80	−1.63	+1.16
KMT-2018-BLG-1354	1.0					
KMT-2018-BLG-2602	0.4	Post Season	17:49:35.29	−21:58:34.32	+6.43	+2.83
OGLE-2018-BLG-1119	0.3	22 Jun 2018	18:00:07.02	−32:22:31.0	−1.38	−4.43
KMT-2018-BLG-1870	0.4					
KMT-2018-BLG-0173	0.4	21 Jun 2018	17:50:11.75	−21:35:40.56	+6.83	+2.91
KMT-2018-BLG-1497	1.0	Post Season	17:44:20.19	−25:58:25.00	+2.38	+1.79
KMT-2018-BLG-1714	1.0	Post Season	17:50:27.27	−33:22:33.82	−3.27	−3.17

The prime fields are those with nominal cadences of $\Gamma = 2\,\rm hr^{-1}$, namely, BLG01, BLG02, BLG03, BLG41, BLG42, and BLG43. We label the (7, 10, 3) remaining fields, with respective nominal cadences $\Gamma = (1.0, 0.4, 0.2)\,\rm hr^{-1}$, as "sub-prime."

The AnomalyFinder (Zang et al. 2022b) identified a total of 173 anomalous events (from an underlying sample of 1728 sub-prime-field events), which it classified as "planet" (17), "planet/binary" (4), "binary/planet" (19), "binary" (126), and "finite source" (7). Among the 126 in the *binary* classification, 35 were judged by eye to be unambiguously nonplanetary in nature. Among the 17 in the *planet* classification, 7 were either previously published (5) or in preparation (2). Among the 4 in the *planet–binary* classification, one was in preparation, and among the 19 in the *binary–planet* classification, one was a previously published planet. None of the events that were classified as *binary* or *finite source* were previously published (or in preparation) planets.

The results from Gould et al. (2022) and this paper can be combined with a detection efficiency analysis (J. Zang et al. 2022, in preparation) to derive the first mass-ratio function based on the KMTNet project. We refer the reader to the introduction of Gould et al. (2022) for the general framework of this approach.

2. Observations

The description of the observations is nearly identical to that in Gould et al. (2022) except that the events analyzed here are derived from 1728 subprime events that were subjected to the AnomalyFinder algorithm compared to 843 prime-field events in Gould et al. (2022). In particular, the KMTNet data are taken from three identical 1.6 m telescopes, each equipped with cameras of 4 deg^2 (Kim et al. 2016) and located in Australia (KMTA), Chile (KMTC), and South Africa (KMTS). When available, our general policy is to include Optical Gravitational Lensing Experiment (OGLE) and Microlensing Observations in Astrophysics (MOA) data in the analysis. However, none of the 9 events analyzed here were alerted by MOA. OGLE data were taken using their 1.3 m telescope with 1.4 deg^2 field of view at Las Campanas Observatory in Chile. For the light-curve analysis, we use only the *I*-band data.

As in Gould et al. (2022), Table 1 gives basic observational information about each event. Column (1) gives the event names in the order of discovery (if discovered by multiple teams), which enables cross identification. The nominal cadences are given in column (2), and column (3) shows the first discovery date. The remaining four columns show the

event coordinates in the equatorial and galactic systems. Events with OGLE names were originally discovered by the OGLE Early Warning System (Udalski et al. 1994; Udalski 2003). KMTNet-named events with alert dates were originally discovered by the KMTNet AlertFinder system (Kim et al. 2018c), while the others were discovered post season by the EventFinder system (Kim et al. 2018a).

To the best of our knowledge, there were no ground-based follow-up observations of any of these events. KMT-2018-BLG-0173 was observed by Spitzer as part of a large-scale microlensing program (Yee et al. 2015), but these data do not show a discernible signal.

The KMT and OGLE data were reduced using a difference image analysis (Tomaney & Crotts 1996; Alard & Lupton 1998), as implemented by each group, i.e., Albrow et al. (2009), Woźniak (2000), respectively.

3. Light-curve Analysis

3.1. Preamble

We present here a compressed version of Section 3.1 of Gould et al. (2022) of the common features of the light-curve analysis. The reader who is interested in more details should consult that work.

All of the events can be initially approximated by 1L1S models, which are specified by three Paczyński (1986) parameters, (t_0, u_0, t_E), i.e., the time of lens-source closest approach, the impact parameter in units of θ_E, and the Einstein timescale,

$$t_{\rm E} = \frac{\theta_{\rm E}}{\mu_{\rm rel}}; \quad \theta_{\rm E} = \sqrt{\kappa M \pi_{\rm rel}}; \quad \kappa \equiv \frac{4\,G}{c^2\,{\rm au}} \simeq 8.14\,\frac{\rm mas}{M_\odot}, \quad (1)$$

where M is the lens mass, $\pi_{\rm rel}$ and $\boldsymbol{\mu}_{\rm rel}$ are the lens-source relative parallax and proper motion, respectively, and $\mu_{\rm rel} \equiv |\boldsymbol{\mu}_{\rm rel}|$. The notation "$nLm$S" means n lenses and m sources. In addition to these 3 nonlinear parameters, there are 2 flux parameters, (f_S, f_B), that are required for each observatory, representing the source flux and the blended flux.

We then search for *static* 2L1S solutions, which generally require 4 additional parameters (s, q, α, ρ), i.e., the planet–host separation in units of θ_E, the planet–host mass ratio, the angle of the source trajectory relative to the binary axis, and the angular source size normalized to θ_E, i.e., $\rho = \theta_{\rm ast}/\theta_{\rm E}$.

We first conduct a grid search with (s, q) held fixed at a grid of values and the remaining 5 parameters allowed to vary in a Monte Carlo Markov Chain (MCMC). After we identify one or

more local minima, we refine these by allowing all 7 parameters to vary.

We often make use of the heuristic analysis introduced by Hwang et al. (2022) and modified by Ryu et al. (2022) based on further investigation in Gould et al. (2022). If a brief anomaly at $t_{\rm anom}$ is treated as due to the source crossing the planet–host axis, then one can estimate two relevant parameters

$$s^{\dagger}_{\pm} = \frac{\sqrt{4 + u^2_{\rm anom}} \pm u_{\rm anom}}{2}; \quad \tan\alpha = \frac{u_0}{\tau_{\rm anom}}, \quad (2)$$

where $u^2_{\rm anom} = \tau^2_{\rm anom} + u^2_0$, and $\tau_{\rm anom} = (t_{\rm anom} - t_0)/t_{\rm E}$. Usually, $s^{\dagger}_+ > 1$ corresponds to anomalous bumps, and $s^{\dagger}_- < 1$ corresponds to anomalous dips. This formalism predicts that if there are two degenerate solutions, $s_{\pm}$, then they both have the same α and that there exists a $\Delta\ln s$ such that

$$s_{\pm} = s^{\dagger}_{\rm pred} \exp(\pm\Delta\ln s), \quad (3)$$

where α and $s^{\dagger}$ are given by Equation (2). To test this prediction in individual cases, we can compare the purely empirical quantity $s^{\dagger} \equiv \sqrt{s_+ s_-}$ with the prediction from Equation (2), which we always label with a subscript, i.e., either $s^{\dagger}_+$ or $s^{\dagger}_-$. This formalism can also be used to find "missing solutions" that have been missed in the grid search, as was done, e.g., for the case of KMT-2021-BLG-1391 (Ryu et al. 2022).

For cases in which the anomaly is a dip, the mass ratio q can be estimated,

$$q = \left(\frac{\Delta t_{\rm dip}}{4\,t_{\rm E}}\right)^2 \frac{s^{\dagger}}{|u_0|} |\sin^3\alpha|, \quad (4)$$

where $\Delta t_{\rm dip}$ is the full duration of the dip. In some cases, we investigate whether the microlens parallax vector

$$\boldsymbol{\pi}_{\rm E} \equiv \frac{\pi_{\rm rel}}{\theta_{\rm E}} \frac{\boldsymbol{\mu}_{\rm rel}}{\mu_{\rm rel}} \quad (5)$$

can be constrained by the data. When both $\pi_{\rm E}$ and $\theta_{\rm E}$ are measured, they can be combined to yield

$$M = \frac{\theta_{\rm E}}{\kappa\pi_{\rm E}}; \qquad D_L = \frac{{\rm au}}{\theta_{\rm E}\pi_{\rm E} + \pi_S}, \quad (6)$$

where D_L is the distance to the lens, and π_S is the parallax of the source.

To model the parallax effects due to Earth's orbital motion, we add two parameters $(\pi_{\rm E,N}, \pi_{\rm E,E})$, which are the components of $\pi_{\rm E}$ in equatorial coordinates. We also add (at least initially) two parameters $\gamma = [(ds/dt)/s, d\alpha/dt]$, where $s\gamma$ are the first derivatives of projected lens orbital position at t_0, i.e., parallel and perpendicular to the projected separation of the planet at that time, respectively. In order to eliminate the unphysical solutions, we impose a constraint on the ratio of the transverse kinetic to potential energy,

$$\beta \equiv \left| \frac{\rm KE}{\rm PE} \right| = \frac{\kappa M_{\odot}{\rm yr}^2}{8\pi^2} \frac{\pi_{\rm E}}{\theta_{\rm E}} \gamma^2 \left(\frac{s}{\pi_{\rm E} + \pi_S/\theta_{\rm E}}\right)^3 < 0.8. \quad (7)$$

It often happens that γ is neither significantly constrained nor significantly correlated with $\pi_{\rm E}$. In these cases, we suppress these 2 degrees of freedom (dof).

In particular, if there are no sharp caustic-crossing features in the light curve, 2L1S events can be mimicked by 1L2S events. Where relevant, we test for such solutions by adding at least 3 parameters $(t_{0,2}, u_{0,2}, q_F)$ to the 1L1S models. These are the time of closest approach and impact parameter of the second source and the ratio of the second to the first source flux in the I band. If either lens-source approach can be interpreted as exhibiting finite source effects, then we must add one or two further parameters, i.e., ρ_1 and/or ρ_2. And, if the two sources are projected closely enough on the sky, one must also consider the source orbital motion.

In a few cases, we make kinematic arguments that solutions are unlikely because their inferred proper motions $\mu_{\rm rel}$ are too small. These arguments rely on the fact that the fraction of events with proper motions less than a given $\mu_{\rm rel} \ll \sigma_{\mu}$ is

$$p(\leqslant\mu_{\rm rel}) = \frac{(\mu_{\rm rel}/\sigma_{\mu})^3}{6\sqrt{\pi}} \rightarrow 4 \times 10^{-3}\left(\frac{\mu_{\rm rel}}{1\ {\rm mas\ yr}^{-1}}\right)^3, \quad (8)$$

where (following Gould et al. 2021) we approximate the bulge proper motions as an isotropic Gaussian with dispersion $\sigma_{\mu} = 2.9\ {\rm mas\ yr}^{-1}$. For example, $p(\leqslant 0.5\ {\rm mas\ yr}^{-1}) = 5 \times 10^{-4}$, and $p(\leqslant 0.1\ {\rm mas\ yr}^{-1}) = 4 \times 10^{-6}$.

3.2. KMT-2018-BLG-0030

Figure 1 shows a low-amplitude ($\Delta I \simeq 0.4$) microlensing event, peaking at $t_0 = 8271.46$ and punctuated by a short bump at $t_{\rm anom} \simeq 8248.0$, i.e., -23.46 days before peak. Assuming that the source is unblended (as is reasonable, see below), the remaining Paczyński (1986) parameters are $u_0 = 0.90$ and $t_{\rm E} = 28$ days. Then $\tau_{\rm anom} = -0.84$, and $u_{\rm anom} = 1.23$. Hence, Equation (2) predicts $s^{\dagger}_+ = 1.79$, and $\alpha = 133°$.

We initially (as usual) conduct the grid search with free blending. This yields a result that is consistent with zero blending, but with a relatively large error, $f_B/f_S \simeq -0.14 \pm 0.14$. The extinction from the KMT website (ultimately derived from Gonzalez et al. 2012, using $A_I = 7\,A_K$), $A_I = 3.25$, implies a dereddened baseline magnitude that is brighter than the clump. The distribution of blending fractions for microlensing events associated with such very bright stars is generally bimodal, i.e., either very low because the apparent bright star is the source or very high because a random field star is the source. Hence, all evidence is consistent with very low blending, and we impose zero blending. The grid search returns only a single solution, whose refinement is shown in Table 2. The resulting $\alpha = 134°.8$ is in reasonable accord with the heuristic prediction, while the value of $s = s_{\rm outer} = 1.58$ would seem to suggest a second solution at $s_{\rm inner} = (s^{\dagger}_+)^2/s_{\rm outer} = 2.03$. That is, Figure 1 shows the source passing "outside" the planetary caustic, so that the "inner/outer degeneracy" (Gaudi & Gould 1997) would seem to suggest a second solution with the source passing inside the planetary caustic. We specifically search for such a solution, in case it was somehow missed by the grid search, by seeding the alternate parameters suggested by the heuristic analysis. We locate an *inner* solution, but it is disfavored by $\Delta\chi^2 = 208$, thus confirming its rejection at the grid-search stage.

As shown in Figure 1, the bump is featureless, so that it could in principle be generated by a second source rather than a second lens (Gaudi 1998). We therefore investigate 1L2S solutions but find that these are excluded by $\Delta\chi^2 = 100.5$.

Such featureless bumps can also, in principle, be caused by a large source passing over one of the two caustics due to a
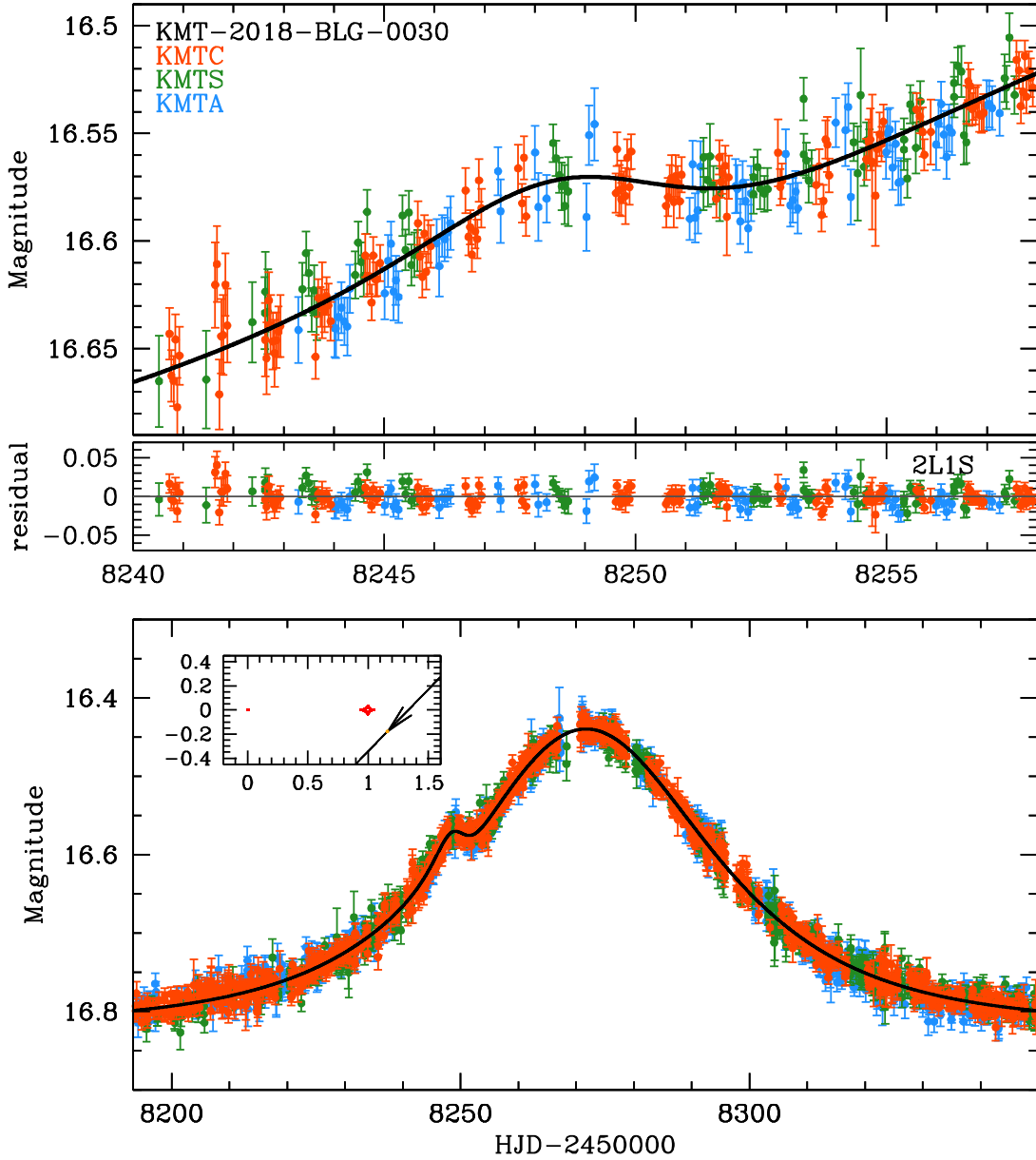
Figure 1. Data (color-coded by observatory) together with the prediction and residuals for the model of KMT-2018-BLG-0030 specified in Table 2. The short *bump* at $t_{anom} = 8248.0$ is caused by the source crossing a ridge extending from the planetary caustic due to a $\log q = -2.5$ super-Jovian mass-ratio planet. See inset.

Table 2
Light-curve Parameters for KMT-2018-BLG-0030

Parameter	
χ^2 / dof	2397.43/2388
$t_0 - 8270$	1.459 ± 0.043
$u_0 \ (10^{-2})$	90.05 ± 0.15
t_E (days)	27.94 ± 0.11
s	1.580 ± 0.013
$q \ (10^{-3})$	2.74 ± 0.30
$\langle \log q \rangle$	-2.563 ± 0.048
α (rad)	2.3521 ± 0.0065
$\rho \ (10^{-3})$	<112
I_S	16.82 ± 0.00

minor-image perturbation (i.e., $s < 1$). As mentioned above, the grid search did not return any such solution. Nevertheless, as a matter of due diligence, we specifically search for these.

However, the best one has extreme negative blending $(f_B/(f_B + f_S)) = -5.5$, and $\Delta\chi^2 = 34$. When we enforce zero blending, the resulting models do not even approximate the observed light curves. Thus, $s < 1$ solutions are ruled out.

Table 2 indicates that this is a super-Jovian mass-ratio planet, $\log q = -2.56$.

Due to the low amplitude of the event (and so, relatively poorly constrained blending in a free fit), we do not attempt to measure the microlens parallax, π_E. Finally, we note that $\rho < 0.112$ (at 2.5σ) is only weakly constrained. We will give quantitative expression to this weakness in Sections 4.1 and 5.1.

KMT-2018-BLG-0030 is one of three previously known planets that are analyzed here for the first time.

3.3. KMT-2018-BLG-0087

Figure 2 shows an approximately 1L1S light curve with Paczyński (1986) parameters $t_0 = 8281.73$, $u_0 = 0.53$, and
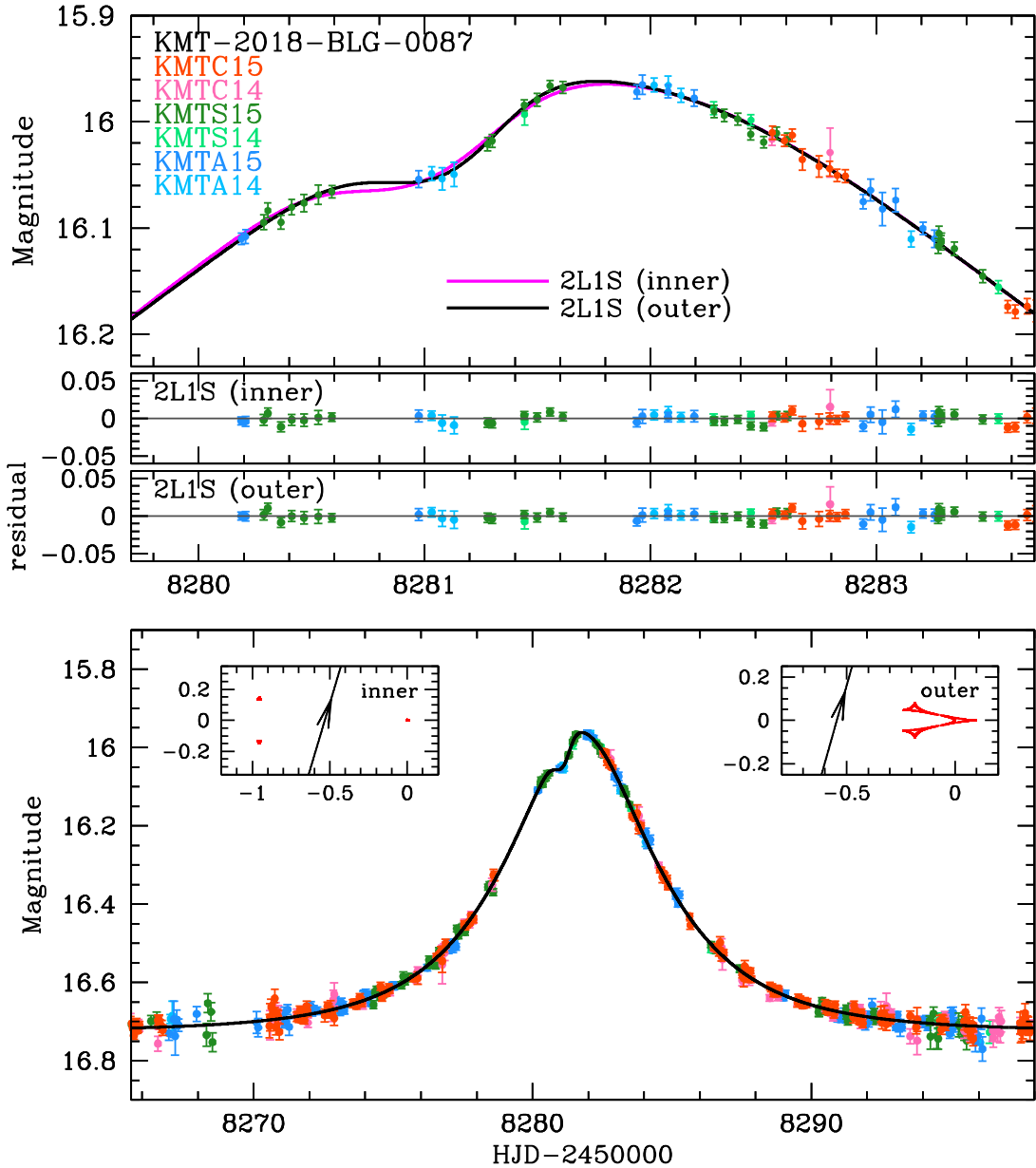
Figure 2. Data (color-coded by observatory and field) together with the predictions and residuals for the models of KMT-2018-BLG-0087 specified in Table 3. The short *dip* at $t_{\rm anom} = 8281.73$ is caused by the source crossing the trough that runs along the minor-image axis due to a $\log q \sim -2.6$ super-Jovian mass-ratio planet. It is subject to the *inner–outer* degeneracy. See insets.

$t_{\rm E} = 4.55$ days, punctuated by a short dip at $t_{\rm anom} = 8281.1$, i.e., $\tau_{\rm anom} = -0.138$. The dip is featureless, while $u_0 \gg |\tau_{\rm anom}|$, indicating a roughly vertical source trajectory. Hence, we expect two solutions (inner–outer degeneracy) with $\alpha = 285°$, and $s_-^{\dagger} = 0.767$. The full duration of the dip is $\Delta t_{\rm dip} = 1.0$ days. Equation (4) then predicts $q = 3.9 \times 10^{-3}$.

The grid search indeed returns two solutions, whose refinement leads to the parameters given in Table 3. These precisely confirm the first two heuristic predictions, with $\alpha = 286°$, and $s^{\dagger} \equiv \sqrt{s_{\rm inner} s_{\rm outer}} = 0.757$, while (as is often the case; Hwang et al. 2022) the mass-ratio prediction is only qualitatively confirmed. The outer solution is significantly (but not overwhelmingly) favored at $\Delta\chi^2 = 5.3$.

This is another super-Jovian mass-ratio planet, with $\log q \simeq -2.65$.

While the constraint on ρ, i.e., $\rho < 0.110$ or $\rho < 0.096$ (at 2.5σ) is very similar to KMT-2018-BLG-0030 (and, as we will see in Section 4, the source sizes are also similar), this constraint will, in contrast to that case, ultimately prove to be significant. This is because the Einstein timescale is much shorter. Indeed, at $t_{\rm E} \sim 4.55$ days, KMT-2018-BLG-0087 is one of the shortest bound-planet events yet detected (Ryu et al. 2021). As we will discuss in Sections 4.2 and 5.2, these characteristics imply that the host is most likely a low-mass star (or possibly brown dwarf) in the bulge.

Although the anomaly is well fitted by a minor-image *dip* and therefore is not expected to be compatible with a 1L2S model, we nevertheless check this possibility as a matter of due diligence. As anticipated, we find that 1L2S is ruled out, with $\Delta\chi^2 = \chi^2(1{\rm L2S}) - \chi^2(2{\rm L1S}) = 100.1$.

Table 3
Light-curve Parameters for KMT-2018-BLG-0087

Parameter	Inner	Outer
χ^2/ dof	3103.66/3087	3098.47/3087
$t_0 - 8280$	1.7373 ± 0.0077	1.7290 ± 0.0079
u_0 (10^{-2})	51.4 ± 1.7	52.8 ± 1.8
t_E (days)	4.607 ± 0.088	4.536 ± 0.090
s	0.638 ± 0.014	0.898 ± 0.024
q (10^{-3})	2.73 ± 0.51	2.17 ± 0.46
$\langle \log q \rangle$	-2.569 ± 0.083	-2.668 ± 0.092
α (rad)	5.001 ± 0.012	4.986 ± 0.012
ρ (10^{-3})	<96	<110
I_S	16.86 ± 0.05	16.82 ± 0.05

Due to the extreme shortness of the event, we do not attempt to measure the microlens parallax, π_E.

Of minor note, KMT-2018-BLG-0087 lies in the very small region of overlap between KMT fields BLG14 and BLG15 and therefore is a rare case of a sub-prime-field event with a $\Gamma = 2 \, \mathrm{hr}^{-1}$ cadence.

3.4. KMT-2018-BLG-0247

Figure 3 shows a short (~ 0.7 day) double-horned profile centered at $t_{anom} = 8305.70$ just after the peak of a normal 1L1S event with parameters $t_0 = 8308.42$, $u_0 = 0.065$, and $t_E = 10.6$ days, yielding $\tau_{anom} = 0.0264$, $u_{anom} = 0.070$, and so $s_+^\dagger = 1.036$, and $\alpha = 68°$.

The grid search returns two solutions, whose refinements are given in Table 4 and whose geometries are shown in Figure 3. Note that both geometries have the source crossing the neck of a resonant caustic, which does not appear to be directly related to either of the degeneracies (inner–outer of Gaudi & Gould 1997; or close–wide of Griest & Safizadeh 1998) that were predicted in advance and that were unified in Equation (2) by Ryu et al. (2022) following the conjecture of Yee et al. (2021). Subsequently, Zhang & Gaudi (2022) investigated the origins of unification at the level of the lens equation. Nevertheless, the two solutions combine to yield $s^\dagger \equiv \sqrt{s_+ s_-} = 1.043$, in excellent agreement with the prediction.

Both solutions imply another super-Jovian mass-ratio planet, $\log q = -2.2$.

Figure 3 shows that only the caustic entrance is resolved. The fact that the source enters the caustic at different angles in the two solutions leads to different values of ρ, which are proportional to the cosine of this angle. Note that if the exit had been resolved by the data, then the degeneracy would have been broken. In this sense, it is accidental.

Due to the short t_E, we do not attempt to measure the microlens parallax, π_E.

KMT-2018-BLG-0247 is one of three previously known planets that are analyzed here for the first time.

3.5. OGLE-2018-BLG-0298

Figure 4 shows a brief bump on the falling wing at $t_{anom} = 8190.6$ of a normal 1L1S event with parameters $t_0 = 8188.74$, $u_0 = 0.021$, and $t_E = 32$ days, yielding $\tau_{anom} = 0.058$, $u_{anom} = 0.062$, and so $s_+^\dagger = 1.031$, and $\alpha = 20°$.

The grid search returns two solutions, whose refinements are shown in Table 5. Based on caustic geometries shown in

Figure 4, these might plausibly be identified as a case of the "inner/outer" degeneracy, although this would be very far from the original conception of Gaudi & Gould (1997). Even so, the parameters $s^\dagger \equiv \sqrt{s_+ s_-} = 1.016$ and $\alpha = 20°$ are in reasonably good agreement with the heuristic prediction. Note that the wide solution has a cusp approach at about 8192.5, which is also preceded by a dip. However, these putative features are not probed by any data. See Figure 4. In this sense, the degeneracy is accidental.

Because the bump is featureless, we check for 1L2S solutions, but we find that these are excluded at $\Delta\chi^2 = 33.7$. In addition, the solution gives $t_{ast,2} = \rho_2 t_E = 0.21$ days, and $q_F = 0.013$, indicating that the second source lies about 7 mag below the clump (see Section 4.4), and so implying $\theta_{ast,2} \sim 0.3 \, \mu$as. These yield $\mu_{rel} = \theta_{ast,2}/t_{ast,2} = 0.55$ mas yr^{-1}, which is quite improbable according to Equation (8). Therefore, we consider the 1L2S models to be decisively excluded.

Given the intermediate timescale, $t_E \sim 32$ days, and moderately faint source, $I_S \sim 20$, it would be unlikely that a full, two-dimensional (2D) parallax could be measured. Nevertheless, a 1D parallax measurement is plausible. For example, Gould et al. (2022) found two such cases. See their Figure 3. Indeed, for the four cases (close $u_0 > 0$, wide $u_0 > 0$, close $u_0 < 0$, wide $u_0 < 0$), we find four very similar, highly elongated error ellipses, with $(\pi_{E,\parallel}, \pi_{E,\perp}, \psi) = (0.00 \pm 0.11, -0.08 \pm 0.63, 272°.1)$, $(-0.02 \pm 0.11, -0.06 \pm 0.68, 272°.0)$, $(0.00 \pm 0.11, -0.19 \pm 0.64, 271°.2)$, and $(-0.02 \pm 0.11, -0.24 \pm 0.64, 271°.5)$, respectively.[13] Here $\pi_{E,\parallel}$, and $\pi_{E,\perp}$ are the minor and major axes of the error ellipse, which are so named because their orientation angle ψ (north through east) is approximately parallel to the projected position of the Sun at the peak of the event. In all cases, the improvement from adding parallax (and orbital motion; see Section 3.1) is $\Delta\chi^2 < 1$ for 4 dof. We find that in all four cases, the numerical contours are well described as Gaussian realizations of the 3-parameter representations listed above.

Nevertheless, the constraint implied by this parallax measurement is moderately significant. As discussed by Han et al. (2016), we are not trying to "detect" parallax: it is known a priori that $\pi_E \equiv \pi_{rel}/\theta_E$ is strictly nonzero. Hence, limits, even 1D limits, on the parallax vector can be constraining when combined with prior information from a Galactic model. We discuss the implementation of these constraints in Section 5.4. Here, we only remark that the remaining parameters change by much less than their error bars, and they would change even less if we were to apply Galactic-model priors to the parallax. Therefore, we report the static-model solutions in Table 5.

This is a sub-Saturn mass-ratio planet, $\log q = -3.7$, the only securely planetary event in this paper to lie in this range. By comparison, among 2018 prime-field unambiguously planetary events that were newly discovered by Anomaly-Finder, there were 5 with $q < 2 \times 10^{-4}$, namely, OGLE-2018-BLG-0383 (Wang et al. 2022), OGLE-2018-BLG-0506, OGLE-2018-BLG-0516, and OGLE-2018-BLG-0977 (Hwang et al. 2022), and OGLE-2018-BLG-1126 (Gould et al. 2022).

---

[13] See Figure 3 of Park et al. (2004) for sign conventions, keeping in mind that OGLE-2018-BLG-0298 peaked before opposition while MOA-2003-BLG-037 peaked after opposition.
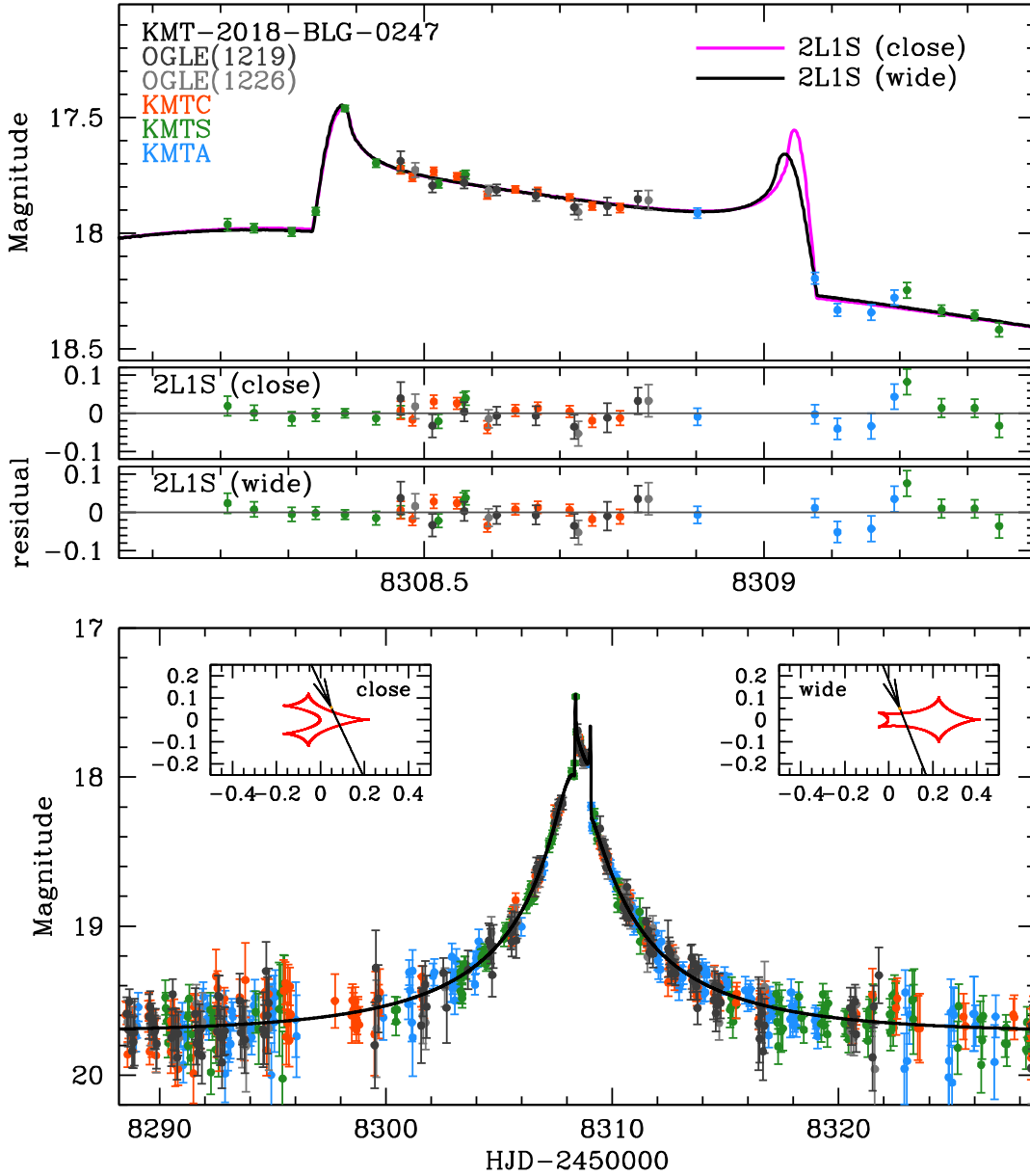
Figure 3. Data (color-coded by observatory and field) together with the predictions and residuals for the models of KMT-2018-BLG-0247 specified in Table 4. The *double-horned profile* centered at $t_{\mathrm{anom}} = 8305.70$ is caused by the source crossing the main body of a resonant caustic due to a $\log q \sim -2.2$ super-Jovian mass-ratio planet. It is subject to a *close–wide degeneracy* (see insets) due to the lack of data on the caustic exit.

3.6. KMT-2018-BLG-2602

Figure 5 shows an approximately 1L1S light curve with parameters $t_0 = 8270.3$, $u_0 = 0.51$, and $t_E = 98$ days, punctuated by a short, smooth bump at $t_{\mathrm{anom}} = 8243.8$, yielding $\tau_{\mathrm{anom}} = -0.27$, and $u_{\mathrm{anom}} = 0.58$, which imply $s_+^{\dagger} = 1.33$, and $\alpha = 118°$.

The grid search returns two solutions, whose refined parameters are shown in Table 6. These agree with the heuristic predictions. In particular $s^{\dagger} \equiv \sqrt{s_+ s_-} = 1.35$. The close solution is favored by $\Delta\chi^2 = 10.4$, and we therefore choose it for our adopted solution. However, the mass ratios of two solutions are nearly identical: this is the Jovian mass-ratio planet, $\log q = -2.8$. Figure 5 shows that the two caustic topologies are related by an *inner–outer degeneracy* in which (as is often the case), the *outer* topology has a resonant caustic.

Table 4
Light-curve Parameters for KMT-2018-BLG-0247

Parameter	Close	Wide
χ^2/ dof	4172.76/4854	4171.10/4854
$t_0 - 8300$	8.4239 ± 0.0065	8.4206 ± 0.0062
u_0 (10^{-2})	6.86 ± 0.40	6.51 ± 0.36
t_E (days)	10.56 ± 0.47	10.67 ± 0.47
s	0.9720 ± 0.0045	1.1182 ± 0.0048
q (10^{-3})	6.28 ± 0.46	7.11 ± 0.56
$\langle \log q \rangle$	-2.203 ± 0.032	-2.149 ± 0.034
α (rad)	1.146 ± 0.014	1.200 ± 0.010
ρ (10^{-3})	1.92 ± 0.19	2.52 ± 0.26
I_S	20.95 ± 0.06	20.96 ± 0.06

Because the bump is featureless, it could in principle be generated by a second source, rather than a second lens. However, we find that 1L2S solutions are excluded at
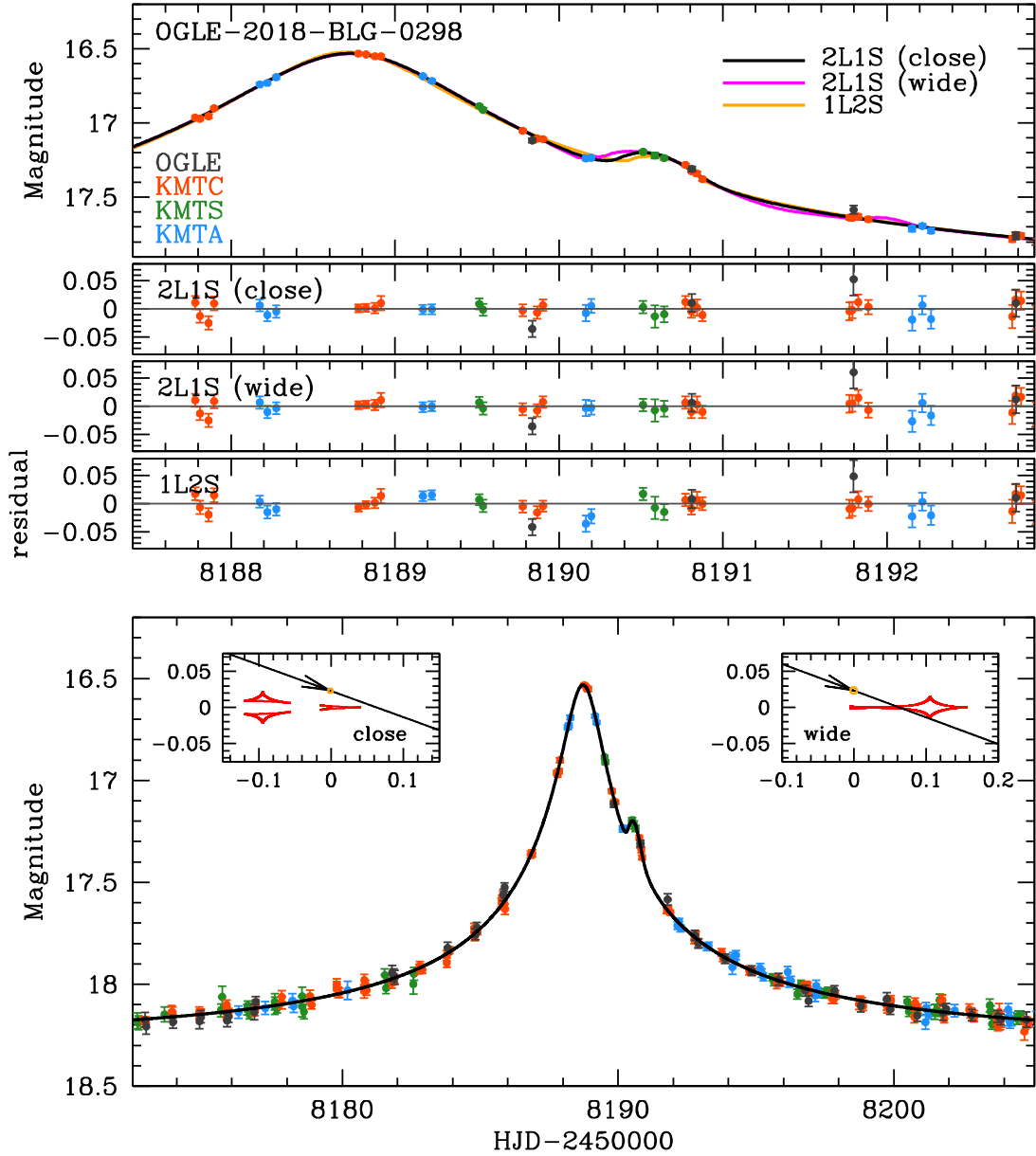
Figure 4. Data (color-coded by observatory) together with the predictions and residuals for the models of OGLE-2018-BLG-0298 specified in Table 5. The short *bump* at $t_{anom} = 8190.6$ is caused by the source crossing a ridge in or extending from the major-image side of the caustic structure due to a $\log q \sim -3.7$ sub-Saturn mass-ratio planet. It is subject to a *close–wide* degeneracy. See insets. The 1L2S model is disfavored by $\Delta\chi^2 = 33.7$ and, in addition, is heavily disfavored by kinematic arguments. Hence, it is excluded.

$\Delta\chi^2 = 30.7$. Moreover, from Table 6, we see that the second-source self-crossing time is $t_{ast,2} \sim 3.9$ days, while the large flux ratio would imply that the second source lies about 7.7 mag below the clump, indicating a second-source radius $\theta_{ast,2} \sim 0.3 \mu$as. Combined, these would imply $\mu_{rel} = \theta_{ast,2}/t_{ast,2} = 0.028$ mas yr^{-1}, which is extraordinarily unlikely. See Equation (8).

By contrast, in the 2L1S solutions, there are only upper limits on ρ, so no such issues arise.

In spite of the long duration of the event, we do not attempt a parallax analysis because the baseline cannot be properly constrained within the 2018 season, and we find small photometric offsets between seasons that would render a multiseason analysis questionable.

KMT-2018-BLG-2602 is one of three previously known planets that are analyzed here for the first time.

3.7. OGLE-2018-BLG-1119

Figure 6 shows an approximately 1L1S light curve with parameters, $t_0 = 8316.0$, $u_0 = 0.43$, and $t_E = 40$ days, punctuated by a small bump before the peak at $t_{anom} = 8310.7$, i.e., with $\tau_{anom} = -0.133$, and so $u_{anom} = 0.45$. These values predict $s_+^\dagger = 1.25$, and $\alpha = 106°$.

The grid search yields two solutions, whose refinements are shown in Table 7. They confirm $s^\dagger \equiv \sqrt{s_+ s_-} = 1.24$, and $\alpha = 107°$. Figure 6 shows that this is an inner–outer degeneracy in which the outer solution has a resonant caustic.

Given the featureless character of the bump (which, in the 2L1S models, is explained by a ridge crossing), we also fit the event with a 1L2S model. Table 7 shows that this is disfavored by $\Delta\chi^2 = 14.0$. In itself, this argues strongly against the 1L2S hypothesis, but does not completely exclude it.

Table 5
Light-curve Parameters for OGLE-2018-BLG-0298

Parameter	Close	Wide	1L2S
$\chi^2/$ dof	3116.68/3258	3119.27/3258	3150.36/3257
$t_0 - 8180$	8.7417 ± 0.0052	8.7387 ± 0.0052	8.7078 ± 0.0048
$t_{0,2} - 8180$			10.646 ± 0.014
$u_0\ (10^{-2})$	2.151 ± 0.077	2.149 ± 0.077	2.317 ± 0.139
$u_{0,2}\ (10^{-2})$			0.147 ± 0.094
$t_{\rm E}$ (days)	32.08 ± 0.98	32.28 ± 0.99	33.35 ± 1.11
s	0.957 ± 0.018	1.079 ± 0.016	
$q\ (10^{-3})$	0.199 ± 0.045	0.137 ± 0.027	
$\langle \log q \rangle$	-3.705 ± 0.099	-3.861 ± 0.081	
α (rad)	0.350 ± 0.006	0.357 ± 0.005	
$\rho\ (10^{-3})$	3.58 ± 0.73	3.98 ± 0.48	<25.50
$\rho_2\ (10^{-3})$			6.20 ± 0.59
$q_F\ (10^{-3})$			13.1 ± 1.4
$I_{\rm S}$	20.67 ± 0.04	20.68 ± 0.04	20.74 ± 0.04

We therefore also investigate the physical plausibility of the 1L2S solution. Table 7 shows that $t_{\rm ast,2} \equiv \rho_2 t_{\rm E} = 1.40 \pm 0.27$ days, and $q_F = 4.2 \times 10^{-3}$. We will see in Section 4.6 that the latter implies that the second source lies ~ 10 mag below the clump, and hence it has $\theta_{\rm ast,2} \sim 0.15\ \mu$as, implying $\mu_{\rm rel} = \theta_{\rm ast,2}/t_{\rm ast,2} \sim 0.039$ mas yr^{-1}. This is extraordinarily improbable, i.e., $p = 2 \times 10^{-7}$, according to Equation (8). Hence, we consider the 1L2S solution to be excluded by the combination of $\Delta\chi^2$ and kinematic arguments.

This is another Jovian-class mass-ratio planet, $\log q = -2.75$.

Due to the event's low amplitude and faint source, we do not attempt a microlens parallax analysis.

3.8. KMT-2018-BLG-0173

Figure 7 shows an approximately 1L1S light curve with parameters of (assuming zero blending) $t_0 = 8348.7$, $u_0 = 0.79$, and $t_{\rm E} = 52$ days, punctuated by a small bump far out on the leading wing at $t_{\rm anom} = 8256$, i.e., with $\tau_{\rm anom} = -1.78$, and so $u_{\rm anom} = 1.95$. At this separation, the planetary caustics are generally small and weak. Hence, it is more likely that the featureless bump is due to the source at least partially enveloping a planetary caustic (either major or minor image), rather than crossing the ridge associated with a major-image caustic. We therefore report both branches of $s_\pm^\dagger$, i.e., $s_-^\dagger = 0.42$, and $s_+^\dagger = 2.37$, with corresponding values of $\alpha_- = 156°$, and $\alpha_+ = 336°$.

The grid search indeed returns two solutions, whose refinements are shown in Table 8, and which are roughly in accord with these predictions. Note that the heuristic formalism naively predicts a second wide solution at $s_{\rm wide,2} = (s^\dagger)^2/s_{\rm wide} = 2.43$. This would basically correspond to the source enveloping the caustic from its left side (as opposed to the right-side envelopment shown in Figure 7). However, the error in s from Table 8 already essentially covers this alternative solution at 1.5σ, and we find that seeding an MCMC with this solution leads to a convergence at the reported solution. Hence, there is a relatively large continuous degeneracy in s, rather than a discrete degeneracy.

Both solutions have Jovian-class mass ratios, $\log q = -3.0$. See Table 8.

Two arguments favor the close solution. First, $\Delta\chi^2 = 11.2$, which is significant but not overwhelming evidence. Second, while the close solution is consistent with small ρ (in particular,

$\rho = 0$ is disfavored by only $\Delta\chi^2 = 3.5$), the wide solution is well localized at $\rho_{\rm wide} \sim 0.125$, corresponding to $t_{\rm ast,wide} \sim 6.5$ days. We will show in Section 4.7 that for the wide solution $\theta_{\rm ast,wide} \sim 6.0\ \mu$as, which would imply $\mu_{\rm rel,wide} = \theta_{\rm ast,wide}/t_{\rm ast,wide} \sim 0.34$ mas yr^{-1}. According to Equation (8), this has a probability $p \sim 1.5 \times 10^{-4}$. (Alternatively, if we force $\rho = 0$, the best-fit solution has an additional $\Delta\chi^2 = 18.0$, which would be formally disfavored by a similar factor, $p = \exp(-(18.0–3.5)/2) = 7 \times 10^{-4}$.) The combination of these two arguments leads us to strongly favor the close over the wide solution.

However, because the anomaly is a featureless bump, we must also check the 1L2S model. See Table 8. This model is disfavored by three different arguments. First, it is disfavored by $\Delta\chi^2 = 10.8$, i.e., very similar to the difference between the close and wide models. If Gaussian statistics applied, this would correspond to $p = 4.5 \times 10^{-3}$, which would effectively settle the matter. However, this χ^2 difference derives from subtle differences in the models over several weeks (see Figure 7), and so could be impacted by equally subtle long-term systematics, which would be difficult to track down. Hence, we look for additional evidence.

The second argument is that the best-fit color of the second source is essentially identical to that of the first source, $\Delta(V - I) \equiv (V - I)_2 - (V - I)_1 \simeq 0$, whereas its magnitude is $-2.5\log(q_F) = 7.5$ mag fainter, and hence should be substantially redder, $\Delta(V - I) \sim 1$. See Section 4.7. That is, if the 2L1S model is correct, the amplitude of the *bump* should be essentially identical in V and I, while for the 1L2S model it should be suppressed by a factor $10^{-0.4\Delta(V-I)} \sim 0.4$. There are 6 V-band points (2 from each observatory) over portions of the bump that deviate from the 1L1S model by at least the order of the V-band error bars (~ 0.03 mag), which track the I-band points (not shown). Unfortunately, this is a weak test because of the paucity of V-band data and the relatively large error bars. We find that if we enforce $\Delta(V - I) = 1$, then χ^2 is only increased by $\Delta\chi^2 = 2.5$. Nevertheless, in contrast to the $\Delta\chi^2 = 10.8$ difference from the I-band fit, this determination is not subject to potential systematic errors from long-term trends in the light curve: it is a purely differential measurement from V and I measurements taken under essentially identical conditions, just 2 minutes apart.

Third, a kinematic argument (similar to the one given above against the 2L1S wide solution) further argues against the 1L2S solution. The flux ratio, $q_F \sim 10^{-3}$, would imply $\theta_{\rm ast,2} \sim 0.3\ \mu$as for the radius of the second source. See Section 4.7. On the other hand, $t_{\rm ast,2} \sim 2.0$ days, implying $\mu_{\rm rel} \sim \theta_{\rm ast,2}/t_{\rm ast,2} = 0.055$ mas yr^{-1}. According to Equation (8), this would have probability $p < 10^{-6}$.

Nevertheless, we note that there is a partial loophole to this argument. While the MCMC is well localized near $\rho_2 \sim 0.04$, solutions with $\rho_2 \sim 0$ are excluded at only (an additional) $\Delta\chi^2 = 6.5$. Thus, a strict comparison of the 2L1S (close) solution and the 1L2S ($\rho_2 = 0$) solution, in effect, favors the former by $\Delta\chi^2 \sim 10.8 + 6.5 - 3.5 = 14.8$. Moreover, if we combine this preference, which is subject to effects of long-term systematics, with the source-color argument above, which is not subject to effects of long-term systematics, we obtain $\Delta\chi^2 \sim 14.8 + 2.5 = 16.3$.

We defer weighing these various pieces of evidence until Section 4.7, where we will bring to bear additional information of the source-star characteristics in these three different models.
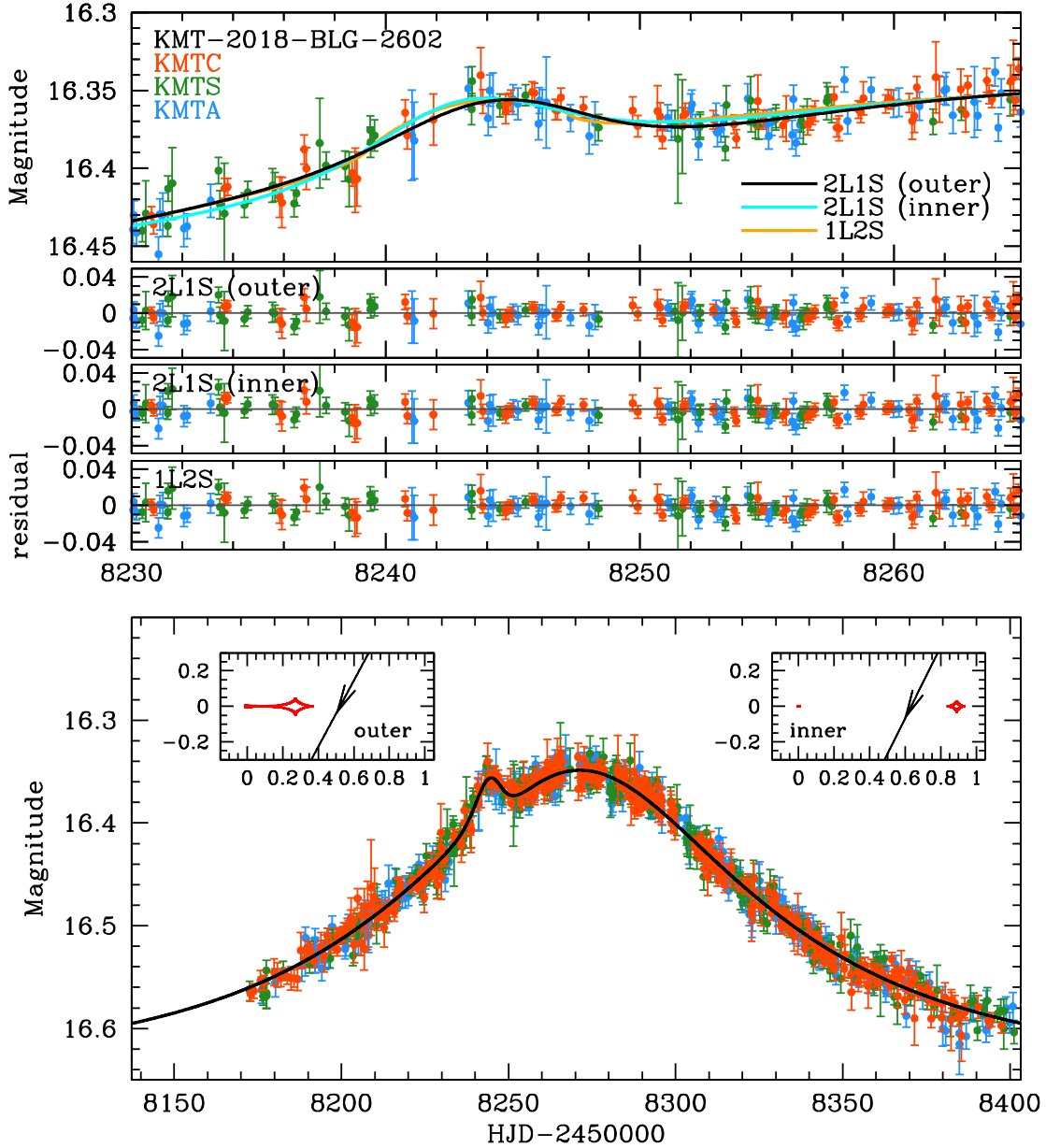
Figure 5. Data (color-coded by observatory) together with the predictions and residuals for the models of KMT-2018-BLG-2602 specified in Table 6. The short *bump* at $t_{anom} = 8243.8$ is caused by the source crossing a ridge extending from the planetary caustic (or planetary wing of the resonant caustic) due to a $\log q \sim -2.8$ Jovian mass-ratio planet. It is nominally subject to an *inner–outer* degeneracy (see insets), but we adopt the *outer* solution because it is favored by $\Delta\chi^2 = 10.3$. The 1L2S model is disfavored by $\Delta\chi^2 = 30.7$ and, in addition, is very heavily disfavored by kinematic arguments. Hence, it is excluded.

3.9. KMT-2018-BLG-1497

Figure 8 shows an approximately 1L1S light curve with parameters, $t_0 = 8229.1$, $u_0 = 0.21$, and $t_E = 31$ days, with a short, possibly structured bump at $t_{anom} = 8233.9$, yielding $\tau_{anom} = +0.155$, and $u_{anom} = 0.26$, which imply $s_+^\dagger = 1.14$, and $\alpha = 59°$.

The grid search returns 3 solutions, whose refinements are shown in Table 9. Two of these approximately correspond to the heuristic prediction, with $s^\dagger = \sqrt{s_+ s_-} = 1.17$, and $\alpha = 55°$. Although the discrepancies are modest in absolute terms, they are significantly larger than is typically the case. Figure 6 shows that, while this is an inner–outer degeneracy, the outer solution has a caustic crossing (which is favored by the early KMTA points), while the inner solution does not. Hence, we do not expect the heuristic formalism to work perfectly.

More importantly, there is a third solution, in which the bump is due to an off-axis cusp approach. See Figure 6. Table 9 shows that the 3 solutions cover a factor 80 range of mass ratios, q, while the full range of χ^2 is only $\Delta\chi^2 = 4.2$. Hence, even if this could be confidently accepted as a planetary event, the planet's characteristics would be extremely uncertain.

Moreover, we find that there is a 1L2S model with $\Delta\chi^2 = 2.1$. See Table 9. Because ρ_2 is not confidently measured for this solution, we cannot make kinematic arguments against it.

Therefore, first, we cannot be confident that this is a planetary event, and second, even if it is, we cannot determine the planet's mass ratio. Therefore, this event should not be cataloged as *planetary*, and, in particular, it should not enter mass-ratio studies.

Parameter	Inner	Outer	1L2S
$\chi^2/$ dof	936.65/920	926.34/920	957.01/919
$t_0 - 8260$	9.95 ± 0.14	10.33 ± 0.15	11.24 ± 0.18
$t_{0,2} - 8260$			-16.59 ± 0.29
$u_0 \, (10^{-2})$	56.5 ± 11.4	51.8 ± 9.3	46.9 ± 8.6
$u_{0,2} \, (10^{-2})$			0.092 ± 0.513
t_E (days)	94.4 ± 16.1	98.7 ± 14.0	108.9 ± 13.7
s	1.532 ± 0.084	1.182 ± 0.065	
$q \, (10^{-3})$	1.62 ± 0.25	1.65 ± 0.27	
$\langle \log q \rangle$	-2.794 ± 0.067	-2.782 ± 0.071	
α (rad)	2.033 ± 0.017	2.057 ± 0.015	
$\rho \, (10^{-3})$	<72	<74	
$\rho_2 \, (10^{-3})$			35.8 ± 6.1
$q_F \, (10^{-3})$			3.44 ± 0.57
I_S	17.88 ± 0.33	18.03 ± 0.28	18.21 ± 0.26

Due to the ambiguous nature of the event, we do not attempt a microlens parallax analysis.

3.10. KMT-2018-BLG-1714

Figure 9 shows an approximately 1L1S light curve with parameters $t_0 = 8318.17$, $u_0 = 0.16$, and $t_E = 3.2$ days, with a short bump defined by just two points at $t_{\rm anom} = 8318.10$, yielding $\tau_{\rm anom} = -0.022$, and $u_{\rm anom} = 0.16$, which imply $s_+^\dagger = 1.08$, and $\alpha = 98°$. The two points were taken in $\sim 1.5''$ seeing, which is good for KMTA, and also very similar to the previous four points. Similarly, the background was low and steady. There is nothing unusual about these points, so we conclude that the increase in recorded flux is of astrophysical origin.

However, a grid search returns three solutions, rather than the usual one or two. Two of these solutions constitute an inner–outer pair, with similar $\alpha = 97°$, and $s^\dagger \equiv \sqrt{s_+ s_-} = 1.09$ to those anticipated from the heuristic analysis (see Table 10). However, the third solution has a completely different topology, in which the bump is generated by an off-axis cusp of a resonant caustic. See Figure 9. The mass ratio of this solution is about 3.5 times larger than those of the other two. While this solution is disfavored by $\Delta\chi^2 = 7.5$, it cannot be definitively excluded on these grounds.

Moreover, such a poorly traced bump could be due to an extra source rather than an extra lens. We find a 1L2S solution with $\Delta\chi^2 = 0.9$. Because ρ_2 is poorly constrained in this solution, we cannot develop arguments against it based on physical considerations, as we could in several other cases. Therefore, we cannot be certain that the anomaly of this event is due to a planet, and we cannot uniquely determine the mass ratio even if it is assumed to be a planet.

Hence, we specifically counsel against cataloging this event as planetary, and, in particular, we advise against it being used in mass-ratio studies.

Due to the ambiguous nature of the event, we do not attempt a microlens parallax analysis.

4. Source Properties

If ρ can be measured from the light curve, then one can use standard techniques (Yoo et al. 2004) to determine the angular source radius, $\theta_{\rm ast}$, and so infer θ_E and $\mu_{\rm rel}$:

$$\theta_E = \frac{\theta_{\rm ast}}{\rho}; \qquad \mu_{\rm rel} = \frac{\theta_E}{t_E}. \qquad (9)$$

However, in contrast to the majority of published by-eye discoveries (but similarly to most of new AnomalyFinder discoveries reported in Zang et al. 2021, 2022b; Hwang et al. 2022; Gould et al. 2022), most of the planetary events reported in this paper have only upper limits on ρ, and these limits are mostly not very constraining. As discussed by Gould et al. (2022), in these cases, $\theta_{\rm ast}$ determinations are not likely to be of much use, either now or in the future. Nevertheless, the source color and magnitude measurement that are required inputs for these determinations may be of use in the interpretation of future high-resolution observations, either by space telescopes or adaptive optics (AO) on large ground-based telescopes. Hence, like Gould et al. (2022), we calculate $\theta_{\rm ast}$ in all cases.

Our general approach is to obtain pyDIA (Albrow 2017) reductions of KMT data at one (or possibly several) observatory–field combinations. These yield the microlensing light curve and field-star photometry on the same system. We then determine the source color by regression of the V-band light curve on the I-band light curve, and the source magnitudes in I by regression on the best-fit model. While Gould et al. (2022) were able to calibrate these color–magnitude diagrams (CMDs) using published field-star photometry from OGLE-III (Szymański et al. 2011) or OGLE-II (Szymański 2005; Kubiak & Szymański 1997; Udalski et al. 2002), only 2 of the 9 sub-prime-field events in this paper are covered by these catalogs. Hence, for the remaining 7, we work directly in the KMTC pyDIA magnitude system. Because the $\theta_{\rm ast}$ measurements depend only on photometry relative to the clump, they are unaffected by calibration. In the current context, calibration is only needed to interpret the limits on lens light. Where relevant, we carry out an alternative approach to calibration, as we explicitly describe.

We then follow the standard method of Yoo et al. (2004). We adopt the intrinsic color of the clump $(V - I)_{0,\rm cl} = 1.06$ from Bensby et al. (2013) and its intrinsic magnitude from Table 1 of Nataf et al. (2013). We obtain $[(V - I), I]_{S,0} = [(V - I), I]_S + [(V - I), I]_{\rm cl,0} - [(V - I), I]_{\rm cl}$. We convert from V/I to V/K using the VIK color–color relations of Bessell & Brett (1988) and then derive $\theta_{\rm ast}$ using the relations of Kervella et al. (2004a, 2004b) for giant and dwarf sources, respectively. After propagating the errors, we add 5% in quadrature to account for errors induced by the overall method. These calculations are shown in Table 11. Where there are multiple solutions, only the one with the lowest χ^2 is shown. However, the values of $\theta_{\rm ast}$ can be inferred for the other solutions by noting the corresponding values of I_S in the event-parameter tables and using $\theta_{\rm ast} \propto 10^{-I_S/5}$. In any case, these are usually the same within the quoted error bars.

Where relevant, we report the astrometric offset of the source from the baseline object.

Comments on individual events follow.

4.1. KMT-2018-BLG-0030

As noted in Section 3.2, the free-blending fit is consistent with zero blending at the 1σ level, and we therefore enforced zero blending in the fit. We also find that the source position lies < 15 mas from the baseline object (i.e., within the
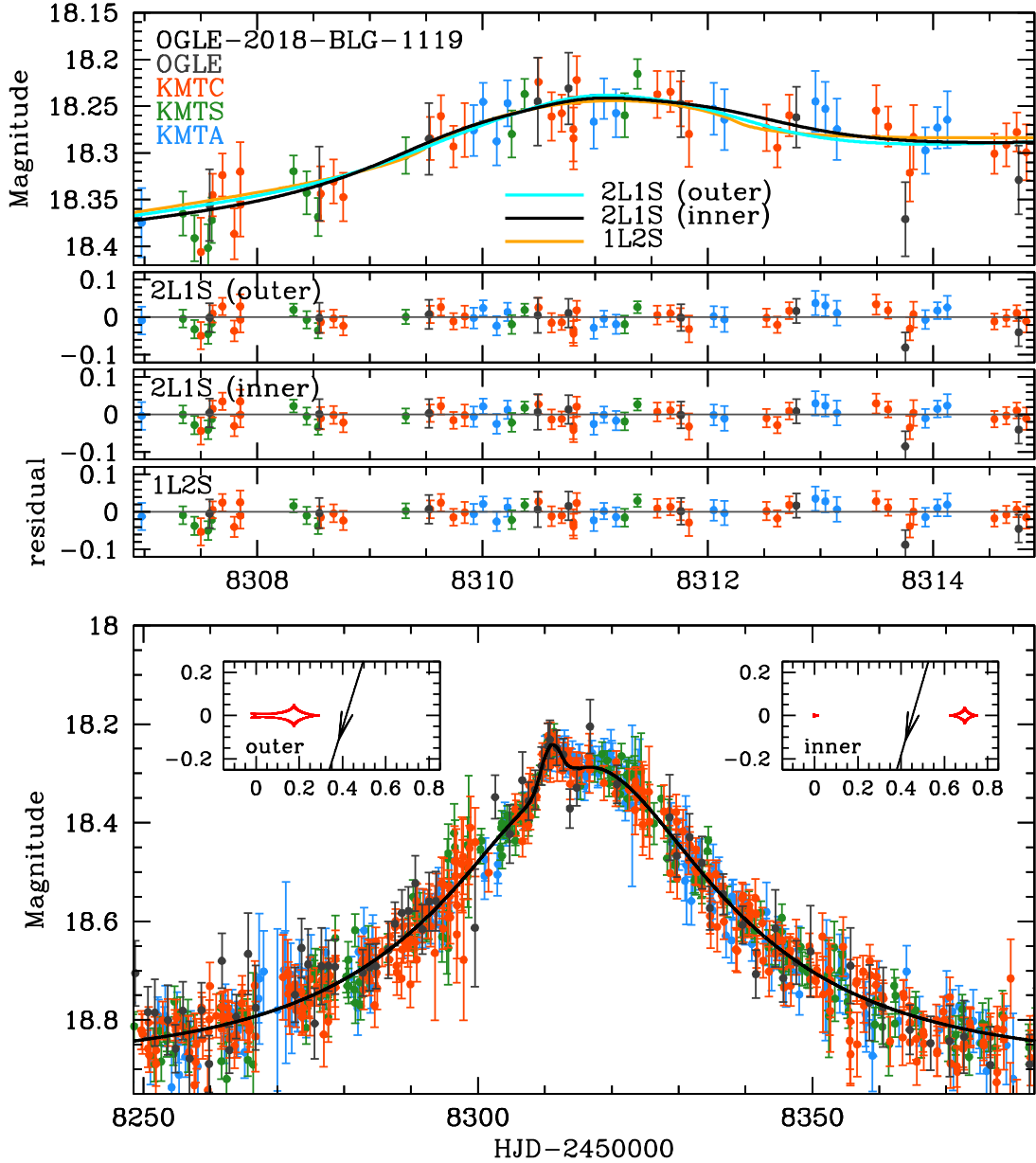
Figure 6. Data (color-coded by observatory) together with the predictions and residuals for the models of OGLE-2018-BLG-1119 specified in Table 7. The short *bump* at $t_{anom} = 8310.7$ is caused by the source crossing a ridge extending from the planetary caustic (or planetary wing of the resonant caustic) due to a $\log q \sim -2.75$ Jovian mass-ratio planet. It is subject to an *inner–outer* degeneracy. See insets. The 1L2S model is disfavored by $\Delta\chi^2 = 14.0$ and, in addition, is very heavily disfavored by kinematic arguments. Hence, it is excluded.

measurement precision), which implies that if there is any blended light, it is almost certainly associated with the event, i.e., from the lens itself, a companion to the lens, or a companion to the source. However, as the source is brighter than the clump (see Figure 10), and the error in the free-blending fit is large, we cannot place useful limits on the lens flux.

The 2.5σ limit $\rho < 0.112$, implies $t_{ast} = \rho t_E < 3.1$ days. Combined with the measurement $\theta_{ast} = 8.5\,\mu$as from Table 11, this implies $\mu_{rel} = \theta_{ast}/t_{ast} > 1.00\,\text{mas yr}^{-1}$. According to Equation (8), this excludes $\sim 0.4\%$ of Galactic events. Hence, while we will include the ρ constraint (or, rather the corresponding constraint $\theta_E > 76\,\mu$as) in the Bayesian analysis of Section 5.1, the only real constraint will be from the measurement of t_E.

We note that Gaia (Gaia Collaboration et al. 2016, 2018) reports a source proper motion of $\mu_S(N, E) = (-7.79, -10.93) \pm (0.45, 0.67)\,\text{mas yr}^{-1}$. If correct, the source would be moving at about $8.3\,\text{mas yr}^{-1}$ relative to the bulge proper-motion centroid. Only an order of 1.6% of bulge sources are moving this fast. However, the Gaia RUWE parameter is 2.2, indicating that the measurement may not be reliable. Hence, because the measurement is both unusual and possibly unreliable, we do not include it in the Bayesian analysis. In any case, because there is no significant constraint on μ_{rel}, the Gaia measurement would not have much effect even if it were included.

4.2. KMT-2018-BLG-0087

The source analysis is overall similar to the case of KMT-2018-BLG-0030 (see Section 4.1). The source position lies

Table 7
Light-curve Parameters for OGLE-2018-BLG-1119

Parameter	Inner	Outer	1L2S
$\chi^2/$ dof	1205.16/1267	1210.73/1267	1219.17/1266
$t_0 - 8310$	5.98 ± 0.13	6.05 ± 0.13	6.28 ± 0.14
$t_{0,2} - 8310$			0.87 ± 0.16
u_0 (10^{-2})	43.5 ± 5.2	40.5 ± 4.6	43.2 ± 5.4
$u_{0,2}$ (10^{-2})			0.59 ± 0.78
t_E (days)	39.3 ± 3.2	41.2 ± 3.3	40.3 ± 3.4
s	1.426 ± 0.047	1.081 ± 0.038	
q (10^{-3})	1.81 ± 0.46	1.70 ± 0.43	
$\langle \log q \rangle$	-2.74 ± 0.11	-2.78 ± 0.11	
α (rad)	1.857 ± 0.016	1.869 ± 0.016	
ρ (10^{-3})	<71	<61	
ρ_2 (10^{-3})			34.8 ± 6.8
q_F (10^{-3})			4.2 ± 1.0
I_S	19.53 ± 0.18	19.64 ± 0.17	19.58 ± 0.19

within ~ 23 mas of the baseline object (consistent with measurement error), while the blended light is consistent with 0 at $<2\sigma$. Hence, if there is blended light, it would again be associated with the event. However, again, because the source is above the clump, while the blend could have at least 10% of the source light, no useful constraint can be put on lens light. Because the color and magnitude of the blend are not well constrained (and because there is no clear evidence that the blend flux is different from 0), we do not display the blended light in Figure 10.

The upper limit $\rho < 0.110$ (or $\rho < 0.096$) is essentially the same as for KMT-2018-BLG-0030, but in this case, it leads to a much shorter limit, $t_{ast} < 0.50$ days, and so to a proper-motion constraint, $\mu_{rel} = \theta_{ast}/t_{ast} > 7.0$ mas yr^{-1}. This is significant and thus can play an important role in the Bayesian analysis in Section 5.2. In fact, we will use the full χ^2 versus ρ envelope, rather than a simple upper limit. Unfortunately, while Gaia has an entry for the source star, it does not report a parallax and proper-motion solution. However, this means that future iterations of the Gaia catalog may report a proper-motion measurement.

4.3. KMT-2018-BLG-0247

The source color measurement using KMTC led to a relatively blue color $(V-I)_{0,S} = 0.51 \pm 0.07$. Hence, we checked the result using KMTS data, but found a consistent result with a substantially larger error, $(V-I)_{0,S} = 0.57 \pm 0.16$. The results reported in Table 11 and shown in Figure 10 are the weighted average of the two measurements. Because of the dearth of such blue stars in the bulge (even at its location on the turnoff), it is likely that the true color is 1σ–1.5σ redder. Nevertheless, we consider that our usual error treatment adequately allows for such variations.

As noted in Section 3.4, the two solutions have substantially different ρ measurements due to the different source angles relative to the caustic entrance. These lead to Einstein-radius and proper-motion measurements,

$$\theta_E = 0.335 \pm 0.045 \text{ mas};$$
$$\mu_{rel} = 11.6 \pm 1.6 \text{ mas yr}^{-1} \qquad \text{(close)}, \qquad (10)$$

and

$$\theta_E = 0.256 \pm 0.034 \text{ mas};$$
$$\mu_{rel} = 8.8 \pm 1.2 \text{ mas yr}^{-1} \qquad \text{(wide)}. \qquad (11)$$

Figure 10 shows that the blend is about 0.6 mag brighter and 0.2 mag bluer than the source. We find that the baseline object is separated by about 180 mas from the source, implying that the blend is about 300 mas from the source. We can robustly say that the lens is fainter than this blend, $I_{L,pyDIA} > I_B = 20.46$ because a lens that was even within a few tenths of a magnitude of I_B would *force* the additional star that is responsible for the astrometric offset to be sufficiently separated to be resolved. However, this limit has almost no impact on bulge lenses because the field extinction, $A_I = 2.99$, implies that this limit only excludes the bulge stars with $M_I \lesssim 2.8$, which are extremely rare. Moreover, the disk lenses that are sufficiently massive to provide this light are already heavily disfavored by the relatively small θ_E in Equations (10) and (11). Nevertheless, we include this limit in Section 5.3 for completeness.

4.4. OGLE-2018-BLG-0298

As for all other events in this paper, the OGLE-2018-BLG-0298 CMD is shown for $[(V-I), I]$. However, while the clump is clearly visible in Figure 10, the lower part of the clump merges into the background noise, which is due to high extinction. In principle, this could make it difficult to properly measure the mean I-band magnitude of the clump. On the other hand, the clump is approximately horizontal (which is the expected behavior provided that there is relatively little differential extinction across the field), implying that the mean $(V-I)$ color of the clump is independent of height and so not significantly affected by growing noise at faint magnitudes.

We therefore measure the height, I_{cl}, (but not the color) of the clump from an $[(I-K), I]$ diagram, which we construct by matching the KMTC pyDIA I-band measurements to the K-band measurements from the VISTA Variables in the Via Lactea catalog (Minniti et al. 2010, 2017). This measurement is illustrated in the *undersized panel* of Figure 11. We emphasize that the only purpose of this panel is to measure I_{cl}, which is then reproduced in Figure 10 and in Table 11.

As shown in Figure 10, the source is blended with a clump giant, compared to which it is about 2.5 mag fainter. The clump giant is separated from the source by about 400 mas, so it is unlikely to be associated with the event. However, it does prevent us from placing any useful limits on the lens light.

From Table 5, it would appear that ρ is measured with tolerable precision, albeit with substantially different error bars for the two solutions. However, the $\chi^2(\rho)$ function is highly non-Gaussian (i.e., not even approximately quadratic). Rather, for, e.g., the close solution, it is approximately flat for $0.003 \lesssim \rho \lesssim 0.0045$; rising linearly, $\Delta\chi^2 \simeq 12$–4000ρ at lower values, and rising almost vertically at higher values. If we simply adopt the best-fit $\rho \sim 3.6 \times 10^{-3}$, then $\theta_E \simeq 0.42$ mas, and $\mu_{rel} \simeq 4.8$ mas yr^{-1}. However, because somewhat lower values of ρ (hence, higher μ_{rel}, which are kinematically favored by Galactic models) have a minimal χ^2 penalty, we will use the actual $\chi^2(\rho)$ function in the Bayesian analysis of Section 5.4, rather than the Gaussian approximation.
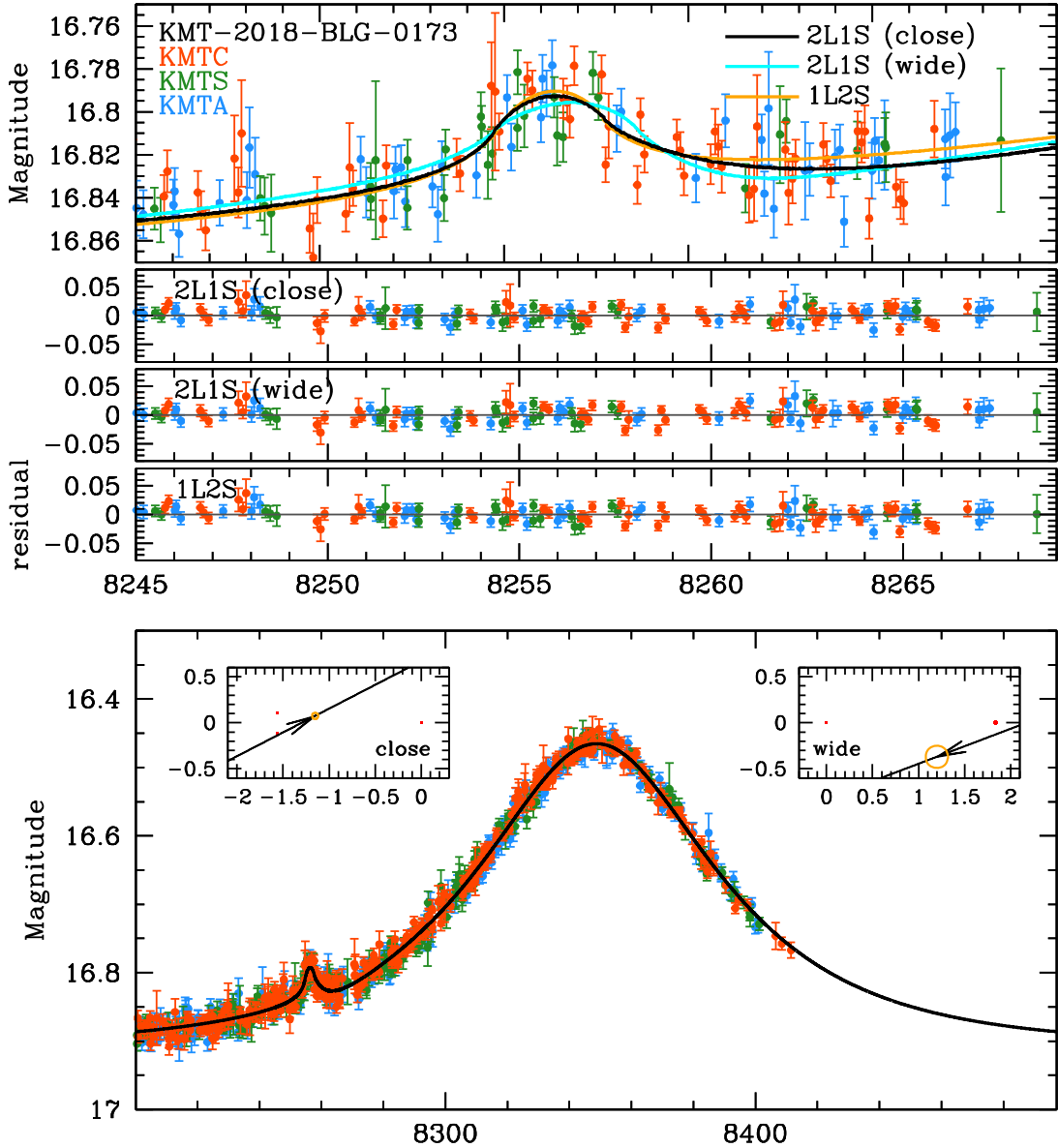
Figure 7. Data (color-coded by observatory) together with the predictions and residuals for the models of KMT-2018-BLG-0173 specified in Table 8. The short *bump* at $t_{anom} = 8256$ has 3 possible explanations: source hitting minor-image caustic (left inset), source hitting major-image caustic (right inset) [both with $\log q = -3.0$], or 1L2S model. The last cannot be decisively rejected based on current data (see Sections 3.8 and 4.7). Therefore, this event should not be cataloged as planetary.

Table 8
Light-curve Parameters for KMT-2018-BLG-0173

Parameter	Close	Wide	1L2S
$\chi^2 /$ dof	927.58/921	938.79/921	938.44/921
$t_0 - 8340$	8.74 ± 0.11	8.65 ± 0.11	8.71 ± 0.11
$t_{0,2} - 8340$			-83.74 ± 0.15
$u_0 \ (10^{-2})$	62.0 ± 4.1	79.7 ± 5.7	83.0 ± 1.2
$u_{0,2} \ (10^{-2})$			1.87 ± 0.89
t_E (days)	62.51 ± 2.90	52.17 ± 2.59	50.48 ± 0.37
s	0.478 ± 0.015	2.314 ± 0.082	
$q \ (10^{-3})$	1.05 ± 0.17	0.97 ± 0.27	
$\langle \log q \rangle$	-2.981 ± 0.069	-3.021 ± 0.125	
α (rad)	5.7990 ± 0.0114	2.7752 ± 0.0087	
$\rho \ (10^{-3})$	<44	125 ± 19	
$\rho_2 \ (10^{-3})$			42.5 ± 7.3
$q_F \ (10^{-3})$			1.04 ± 0.15
I_S	17.46 ± 0.12	16.98 ± 0.14	16.90 ± 0.00

4.5. KMT-2018-BLG-2602

Very similarly to the case of OGLE-2018-BLG-0298 (Section 4.4), the source is blended with a clump giant, although in this case the source is 1.5 mag fainter. In addition, in this case, the source is aligned with the baseline object to within 10 mas, probably indicating that the (clump-giant) blend is a companion to the (subgiant) source. If one were to naively apply the arguments given above for KMT-2018-BLG-0030 and KMT-2018-BLG-0087, one might conclude from the presence of a clump-giant blend that no useful limits could be put on lens light. However, this proves not to be the case (see Section 5.5).

In Table 6, we list a 2.5σ limit $\rho < 0.074$, which considered by itself would imply $\mu_{rel} > 0.13$ mas yr^{-1}, i.e., completely unconstraining according to Equation (8). We check whether there are are additional subtle structures in the $\chi^2(\rho)$ function
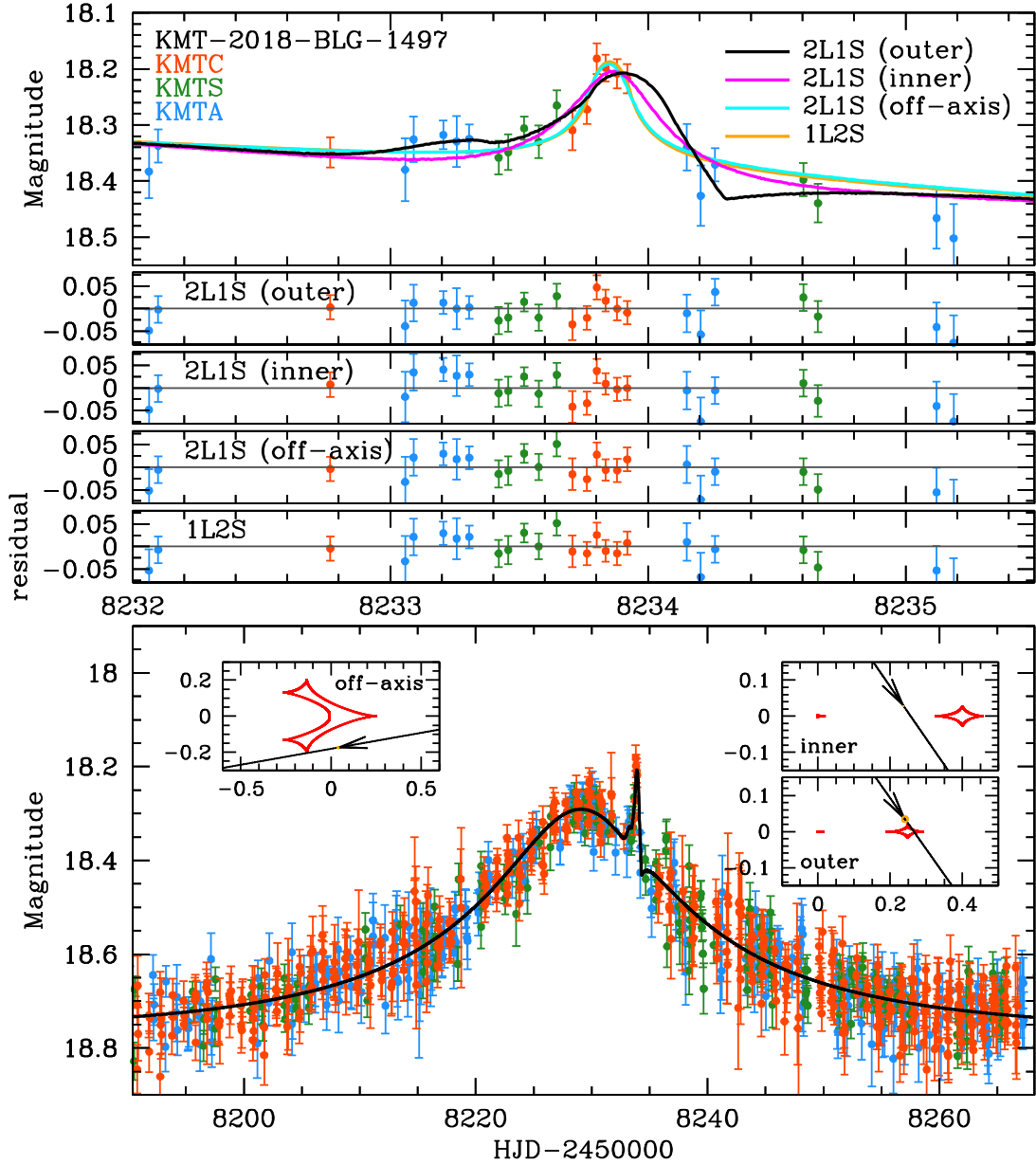
Figure 8. Data (color-coded by observatory) together with the predictions and residuals for the models of KMT-2018-BLG-1497 specified in Table 9. The short *bump* at $t_{anom} = 8233.9$ has 4 possible explanations: 2 from an *inner–outer* degeneracy (right insets), 1 from an off-axis cusp approach (left inset) [together with $-3.7 \lesssim \log q \lesssim -1.8$], or 1L2S model. The last has $\Delta\chi^2 = 2.1$, and there are no other arguments against it. Therefore, this event should not be cataloged as planetary.

that might provide additional constraints. However, we find, on the contrary, that all values $0 < \rho < 0.05$ are consistent with the minimum at 1σ. Hence, we simply adopt the Table 6 2.5σ limit in the Bayesian analysis in Section 5.5.

For completeness, we note that Gaia lists a proper-motion measurement for the baseline object of $\mu_{base}(N, E) = (-9.89 \pm 0.12, -2.37 \pm 0.19)$ mas yr^{-1}. If, as appears very likely, the baseline object is composed of the source and its companion, then the source proper motion is given by $\mu_S = \mu_{base}$. This source proper motion would then be about $|\Delta\mu| \sim 4.7$ mas yr^{-1}, i.e., 1.6σ from the bulge mean. However, we do not include this measurement in the analysis for two reasons. First, we cannot be certain that the blend is a companion to the source. Second, in the absence of significant

constraints on μ_{rel}, knowledge of the source proper motion plays a very little role.

4.6. OGLE-2018-BLG-1119

OGLE-2018-BLG-1119 is one of only two events that are analyzed in this paper that are covered by OGLE-III. We therefore provide calibrated photometry for it in Figure 11 and in Table 11.

Moreover, this also allows us to compare the field-star astrometry of pyDIA KMTC to that of OGLE-III. Both catalogs find a neighbor roughly due east of the source, at about 760 mas for OGLE-III and 870 mas for KMTC. However, the two catalogs divide the light between these two stars differently: OGLE-III puts 75% of the total light in the source,

Table 9
Light-curve Parameters for KMT-2018-BLG-1497

Parameter	Inner	Outer	Off-axis Cusp	1L2S
$\chi^2/$ dof	2466.85/2457	2463.63/2457	2467.78/2457	2465.74/2456
$t_0 - 8220$	9.22 ± 0.11	9.14 ± 0.11	8.07 ± 0.12	8.98 ± 0.12
$t_{0,2} - 8220$				13.854 ± 0.026
$u_0 \ (10^{-2})$	22.1 ± 2.3	21.0 ± 1.8	18.4 ± 1.3	19.2 ± 2.4
$u_{0,2} \ (10^{-2})$				0.23 ± 0.14
t_E (days)	30.6 ± 2.3	31.9 ± 2.0	34.0 ± 1.9	34.2 ± 2.9
s	1.227 ± 0.019	1.128 ± 0.012	0.928 ± 0.005	
$q \ (10^{-3})$	0.75 ± 0.24	0.21 ± 0.07	17.38 ± 2.48	
$\langle \log q \rangle$	-3.127 ± 0.136	-3.684 ± 0.139	-1.763 ± 0.063	
α (rad)	0.971 ± 0.020	0.955 ± 0.019	2.971 ± 0.045	
$\rho \ (10^{-3})$	<8.6	7.8 ± 1.7	< 7.8	
$\rho_2 \ (10^{-3})$				<6.7
$q_F \ (10^{-3})$				4.2 ± 1.6
I_S	20.79 ± 0.13	20.87 ± 0.11	21.03 ± 0.09	21.00 ± 0.15

whereas for KMTC this figure is 33%. Furthermore, the combined light of the two stars is 0.32 mag brighter in KMTC (after alignment of the two systems).

From this comparison, we can robustly conclude that the baseline object is semiresolved from its neighbor, but we cannot tell, a priori, whether OGLE-III or KMTC has a more accurate assessment of the brightness of the baseline object. Nevertheless, it is striking that the KMTC baseline-object measurement is nearly identical to the source flux as determined from the light-curve model, implying that it is quite possible that there is very little blended light, e.g., from the lens. Therefore, we do not show any blend in the CMD.

On the other hand, we cannot rule out that the OGLE-III measurement is actually correct. Therefore, we must place a conservative limit on lens light, namely that $I_L > 19.7$, i.e., roughly as bright as the source.

In Table 7, we show only an upper limit for the ρ measurement. This is because, while there is a clearly defined minimum in $\chi^2(\rho)$ at the 1σ level, all values $\rho < 0.065$ are consistent at $\Delta\chi^2 < 4$. If we, for the moment, take the best-fit value $\rho = 0.045$ seriously, then $t_{\rm ast} = 1.84$ days, so that $\mu_{\rm rel} = \theta_{\rm ast}/t_{\rm ast} = 0.14$ mas yr^{-1}, which is extraordinarily unlikely according to Equation (8). Therefore, the apparent 1σ *measurement* of ρ is almost certainly due to a statistical fluctuation or minor systematics. Hence, in Section 5.6, we use only the upper limit $\rho < 0.071$ (or $\rho < 0.061$).

4.7. KMT-2018-BLG-0173

Recall from Section 3.8 that it was difficult to distinguish among three possibilities: 2L1S (close), 2L1S (wide), and 1L2S. In brief, 2L1S (close) was preferred over the other two by $\Delta\chi^2 \sim 11$. Moreover, both the 2L1S (wide) and 1L2S solutions had reasonably well-determined ρ values that would imply improbably low values of $\mu_{\rm rel}$. Note that the best-fit value for $\theta_{\rm ast}$ given in Table 11 is (as always) for the lowest-χ^2 solution. Hence, $\theta_{\rm ast,wide} = \theta_{\rm ast,close} \times 10^{0.48/5} = 5.45 \ \mu{\rm as}$.

Nevertheless, we found that these proper-motion arguments could be evaded in both cases by accepting a modest χ^2 penalty for enforcing $\rho = 0$, which would thereby accommodate much higher (including very plausible) proper motions.

An additional color-based argument was given against 1L2S, but unfortunately this was statistically weak; $\Delta\chi^2 = 2.5$.

Here, we show that the CMD, when combined with the astrometric measurements, argues in exactly the opposite direction, i.e., that both the 2L1S (wide) and 1L2S solutions are strongly preferred over the 2L1S (close) solution.

The argument concerns the blended light. The first point is that, in the 2L1S (close) solution, the blended light is about equal to that of the source, while in both the 2L1S (wide) and 1L2S solutions, the blended light is consistent with 0 at 1σ. This difference becomes important because the measured offset between the source and the baseline object is just 7 mas, i.e., within the measurement error. This close alignment implies that the blended light (if any) is almost certainly associated with the lens, either the lens itself, a companion to the lens, or a companion to the source. (The usual argument against field-star contamination is made even stronger by the fact that the surface density of clump stars, which are proxies for the giant stars of direct interest here, is only half that of Baade's Window, and so a factor 3–5 smaller than that of typical events.[14])

Figure 10 shows the source and blend positions for the 2L1S close solution in blue and green, respectively. The magenta point shows the baseline object, which would be the source position for either of the other solutions, assuming no blending. Thus, in the 2L1S close solution (but for neither of the others), the blend would be (within measurement error) a twin of the source, and thus almost certainly a companion to the source of virtually identical mass in a very rapid phase of stellar evolution.

Because each of these three solutions has some very improbable feature, we do not regard it as possible to confidently choose among them based on current evidence. It is possible that additional data, such as AO imaging and/or spectroscopy on large telescopes, will eventually resolve the issue. However, at present, we believe that this event should not be cataloged as *planetary*.

4.8. KMT-2018-BLG-1497

In Section 3.9, we showed that there are three different planetary solutions for KMT-2018-BLG-1497, with mass ratios, q, spanning 2 orders of magnitude, plus a 1L2S solution, all within $\Delta\chi^2 \lesssim 4$. Thus, the $\theta_{\rm ast}$ evaluation in Table 11 and the CMD in Figure 11 (both, as usual, for the lowest-χ^2 solution) are shown only for completeness: they could become of interest if future observations can distinguish among these solutions.

---

[14] We evaluate this using the measurements by Nataf et al. 2013 in the neighborhood of the reflection point $(l, b) \to (l, -b)$ because the northern bulge is not well covered in that study.

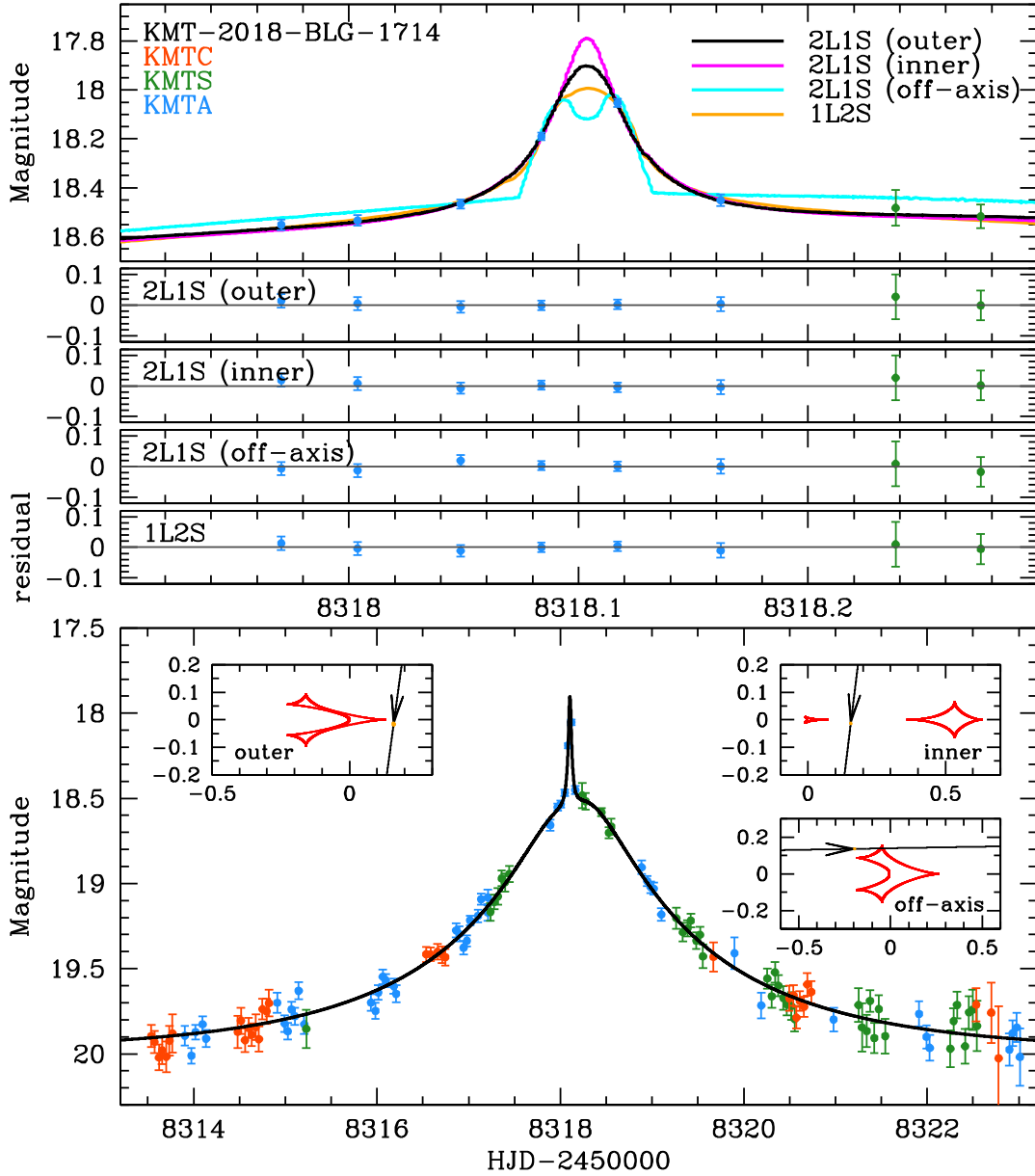**Figure 9.** Data (color-coded by observatory) together with the predictions and residuals for the models of KMT-2018-BLG-1714 specified in Table 10. The short *bump* at $t_{anom} = 8318.10$ has 4 possible explanations: 2 from an *inner–outer* degeneracy (top insets), 1 from an off-axis cusp approach (lower right inset) [together with $-2.4 \lesssim \log q \lesssim -1.8$], or 1L2S model. The last has $\Delta\chi^2 = 0.9$, and there are no other arguments against it. Therefore, this event should not be cataloged as planetary.

4.9. KMT-2018-BLG-1714

In Section 3.10, we showed that, for KMT-2018-BLG-1714, there is a 1L1S solution within $\Delta\chi^2 < 1$ of the best planetary solution. In addition, there was a factor 3.5 degeneracy in q at $\Delta\chi^2 \sim 7$. Thus, as for KMT-2018-BLG-1497, the θ_{ast} evaluation in Table 11 and the CMD in Figure 11 are shown only for completeness because they could become of interest if future observations can distinguish among these solutions.

5. Physical Parameters

To make Bayesian estimates of the lens properties, we follow the same procedures as described in Section 5 of Gould et al. (2022). We refer the reader to that work for details.

In Table 12, we present the resulting Bayesian estimates of the host mass M_{host}, the planet mass M_{planet}, the distance to the

lens system D_L, and the planet–host projected separation $a_\perp$. For the majority of events, there are two or more competing solutions. For these cases (following Gould et al. 2022), we show the results of the Bayesian analysis for each solution separately, and we then show the *adopted* values below these. For M_{host}, M_{planet}, and D_L, these are simply the weighted averages of the separate solutions, where the weights are the products of the two factors at the right side of each row. The first factor is simply the total weight from the Bayesian analysis. The second is $\exp(-\Delta\chi^2/2)$ where $\Delta\chi^2$ is the χ^2 difference relative to the best solution. For $a_\perp$, we follow a similar approach provided that either the individual solutions are strongly overlapping or one solution is strongly dominant. If neither condition were met, we would enter *bimodal* instead. However, in practice, this condition is met for all 4 events for which there is potentially an issue.

Table 10
Light-curve Parameters for KMT-2018-BLG-1714

Parameter	Inner	Outer	Off-axis Cusp	1L2S
$\chi^2/$ dof	2033.08/2028	2032.94/2028	2040.35/2028	2033.80/2027
$t_0 - 8310$	8.168 ± 0.012	8.170 ± 0.012	8.280 ± 0.015	8.179 ± 0.014
$t_{0,2} - 8310$				8.1047 ± 0.0025
$u_0 \,(10^{-2})$	15.7 ± 2.0	16.2 ± 2.2	14.4 ± 1.3	18.9 ± 3.1
$u_{0,2} \,(10^{-2})$				0.056 ± 0.184
t_E (days)	3.21 ± 0.29	3.17 ± 0.30	3.52 ± 0.22	3.12 ± 0.28
s	1.293 ± 0.038	0.921 ± 0.028	0.974 ± 0.004	
$q \,(10^{-3})$	3.97 ± 1.67	3.68 ± 1.74	12.83 ± 2.43	
$\langle \log q \rangle$	-2.40 ± 0.14	-2.43 ± 0.15	-1.89 ± 0.081	
α (rad)	1.693 ± 0.024	1.694 ± 0.024	0.030 ± 0.042	
$\rho \,(10^{-3})$	<15.6	<16.8	<10.3	
$\rho_2 \,(10^{-3})$				<12.4
$q_F \,(10^{-3})$				13.5 ± 2.6
I_S	20.56 ± 0.17	20.54 ± 0.17	20.72 ± 0.12	20.50 ± 0.19

We present Bayesian analyses for 6 of the 9 events, but not for KMT-2018-BLG-0173, KMT-2018-BLG-1497, and KMT-2018-BLG-1714, for which we cannot distinguish between competing interpretations of the event. See Sections 3.8, 3.9, and 3.10. Figures 12 and 13 show histograms for $M_{\rm host}$ and D_L for these 6 events.

5.1. KMT-2018-BLG-0030

For KMT-2018-BLG-0030, there is only one light-curve solution. As discussed in Sections 3.2 and 4.1, while we include two constraints, $t_E = 27.94 \pm 0.11$ days, and $\theta_E > 76 \,\mu$as; only the first of these has practical importance. For reasons discussed in Section 3.2, we do not include the Gaia measurement of μ_S as a constraint, although (as also discussed there) doing so would have had very little effect. In Section 6.3, we develop additional support for this decision.

As illustrated by Figure 12, the relatively long timescale somewhat favors more massive hosts, but the lens-distance distribution primarily just reflects the Galactic prior.

5.2. KMT-2018-BLG-0087

For KMT-2018-BLG-0087, there are two solutions. For each, there are two constraints, one on t_E (as given in Table 3) and the other on θ_E. As discussed in Section 3.3, the seemingly crude limit on ρ is significant due to the short t_E. Hence, as discussed in Section 3.3, the profile $\chi^2(\rho)$ actually matters. Therefore, we implement the θ_E constraint by, for each simulated event with Einstein radius θ_E, first evaluating $\rho = \theta_{\rm ast}/\theta_E$ (where $\theta_{\rm ast} = 9.53 \,\mu$as), and then assigning a weight

$$w_{\theta_E} = \frac{\exp[-\chi^2(\rho)/2]}{Q}; \qquad Q \equiv \int_0^\infty d\rho \, \exp[-\chi^2(\rho)/2], \quad (12)$$

where

$$\chi^2_{\rm inner}(\rho) = \left(\frac{\rho}{0.044}\right)^2;$$

$$\chi^2_{\rm outer}(\rho) = \left(\frac{\rho}{0.080}\right)^2 \quad (\rho < 0.09);$$

$$\chi^2_{\rm outer}(\rho) = \frac{81}{64} + 5\left(\frac{\rho - 0.09}{0.02}\right)^2 \quad (\rho > 0.09), \quad (13)$$

with $Q_{\rm inner} = 0.044\sqrt{\pi/2} = 0.055$, and $Q_{\rm outer} = 0.081$.

The host mass is peaked near the star–brown-dwarf boundary, while the lens distance is strongly dominated by the bulge population. See Figure 12. The physical reason for this is that the combination of the modeling constraints and the Galactic priors strongly favors events with small $\theta_E = \sqrt{\kappa M \pi_{\rm rel}}$ (so, low M and low $\pi_{\rm rel}$). That is, by itself, the 2.5σ limit on ρ would only imply a lower limit: $\theta_E > 0.086$ mas, but substantially larger θ_E would lead to high proper motions that are heavily disfavored by the Galactic priors.

5.3. KMT-2018-BLG-0247

For KMT-2018-BLG-0247, there are two solutions. For each, there are three constraints: the first on t_E (as given in Table 4), the second on θ_E (as given in Equations (10) and (11)), and the third on lens light $I_{L,\rm pyDIA} > 20.46$ (as described in Section 4.3). In order to put this limit on a calibrated scale, we estimate $I_{\rm calib} - I_{\rm pyDIA} = I_{\rm cl,calib} - I_{\rm cl,pyDIA} = I_{\rm cl,0} + A_I - I_{\rm pyDIA} = -0.03$, where $I_{\rm cl,0}$ and $I_{\rm pyDIA}$ are from Table 11, and $A_I = 2.99$ is from the KMT webpage as described in Section 3.2. Therefore, the calibrated limit is $I_L > 20.43$.

The host distributions (Figure 12) are dominated by bulge M dwarfs. Kim et al. (2021b) showed that for measured proper motions $\mu_{\rm rel} \lesssim 10 \,{\rm mas}\,{\rm yr}^{-1}$, Bayesian mass estimates depend almost entirely on the θ_E measurement. Our results for both the close and wide solutions (which differ by a factor 1.3) are in good accord with the predictions from their Figures 6 and 7. Note that, as anticipated in Section 4.3, the lens-flux constraint plays almost no role because the other constraints already favor very faint lenses.

5.4. OGLE-2018-BLG-0298

For OGLE-2018-BLG-0298, there are two solutions. For each, there are three constraints. The first, on t_E, is given in Table 5, while each of the other two, on θ_E and π_E, require additional discussion.

As mentioned in Section 4.4, for the close solution, $\chi^2(\rho)$ is both fairly broad and highly non-Gaussian. Therefore, as in the case of KMT-2018-BLG-0087 (Section 5.2), we employ Equation (12) by directly characterizing $\chi^2(\rho)$:

$$\chi^2_{\rm close}(\rho) = 12 - 4000\rho \quad (\rho < 0.003);$$
$$= 0 \quad (0.003 < \rho < 0.0045);$$
$$= 24000\rho - 108 \quad (\rho < 0.0045);$$

Table 11
CMD Parameters

Name	$(V-I)_S$	$(V-I)_{cl}$	$(V-I)_{S,0}$	I_S	I_{cl}	$I_{cl,0}$	$I_{S,0}$	$\theta_*(\mu as)$
KMT-2018-BLG-0030	3.57 ± 0.03	3.49 ± 0.03	1.14 ± 0.04	16.88 ± 0.01	17.40 ± 0.03	14.45	13.93 ± 0.03	8.478 ± 0.526
KMT-2018-BLG-0087	3.98 ± 0.05	3.67 ± 0.03	1.37 ± 0.06	16.97 ± 0.02	17.45 ± 0.03	14.44	13.96 ± 0.05	9.529 ± 0.632
KMT-2018-BLG-0247	3.11 ± 0.06	3.65 ± 0.02	0.52 ± 0.07	21.03 ± 0.03	17.43 ± 0.03	14.41	18.01 ± 0.04	0.641 ± 0.055
OGLE-2018-BLG-0298	4.36 ± 0.06	4.65 ± 0.03	0.77 ± 0.07	20.74 ± 0.03	18.55 ± 0.06	14.53	16.72 ± 0.07	1.513 ± 0.142
KMT-2018-BLG-2602	2.93 ± 0.07	2.93 ± 0.03	1.06 ± 0.08	18.22 ± 0.03	16.60 ± 0.05	14.26	15.88 ± 0.06	3.207 ± 0.310
OGLE-2018-BLG-1119	1.64 ± 0.11	2.00 ± 0.03	0.70 ± 0.12	19.50 ± 0.03	15.73 ± 0.05	14.52	18.29 ± 0.06	0.681 ± 0.095
KMT-2018-BLG-0173	3.01 ± 0.06	3.05 ± 0.03	1.02 ± 0.07	17.67 ± 0.02	16.96 ± 0.08	14.25	14.96 ± 0.08	4.371 ± 0.371
KMT-2018-BLG-1497	3.13 ± 0.10	3.26 ± 0.03	0.93 ± 0.11	20.96 ± 0.03	17.45 ± 0.04	14.36	17.87 ± 0.05	1.110 ± 0.166
KMT-2018-BLG-1714	2.60 ± 0.11	2.41 ± 0.03	1.25 ± 0.12	20.08 ± 0.03	16.25 ± 0.05	14.59	18.42 ± 0.06	1.226 ± 0.114

Note. $(V-I)_{cl,0} = 1.06$.

$$\chi^2_{\text{wide}}(\rho) = \left(\frac{1000\rho - 3.98}{0.48}\right)^2; \qquad (14)$$

with $Q_{\text{close}} = 2.09 \times 10^{-3}$, and $Q_{\text{wide}} = \sqrt{2\pi}\,0.48 \times 10^{-3} = 1.20 \times 10^{-3}$.

To incorporate the parallax measurement, we could in principle double the number of solutions from 2 to 4, and then average together the Bayesian results from the two close solutions and from the two wide solutions. However, an inspection of the parallax solutions given in Section 3.5 (in principal-axis format) shows that the pair of close (or wide) solutions differ by much less than their errors, and the error ellipses are also extremely similar. These are natural consequences of the fact that $u_0 \ll 1$. Hence, it makes more sense to average these solutions, before applying the Bayesian results than after. Next, we notice that the parallax solutions for the close and wide solutions for a given sign of u_0 are even more similar than are, e.g., the two close solutions. Hence, for simplicity, we simply average together the four solutions (in equatorial coordinates) to obtain

$$a_{i,0} = \begin{pmatrix} \pi_{E,N,0} \\ \pi_{E,E,0} \end{pmatrix} = \begin{pmatrix} -0.1433 \\ +0.0079 \end{pmatrix};$$

$$c_{ij} = \begin{pmatrix} 0.4287 & 0.0127 \\ 0.0127 & 0.0128 \end{pmatrix}, \qquad (15)$$

and we then derive the parallax weight,

$$w_{\text{par}} = \frac{\exp(-\sum_i\sum_j(a_i - a_{i,0})b_{ij}(a_j - a_{j,0})/2)}{\sqrt{2\pi \det(b)}}, \qquad (16)$$

where $b \equiv c^{-1}$, and $a_i = (\pi_{E,N}, \pi_{E,E})_i$ of the simulated event, i.

The results of the Bayesian analysis can be qualitatively understood by considering a *typical* value of $\rho \sim 4 \times 10^{-3}$; hence $\theta_E \sim 0.38$ mas, and $\mu_{\text{rel}} \sim 4$ mas yr^{-1}. If there were no parallax information, then the argument of Kim et al. (2021b) would lead to a mass estimate $M \sim 0.44\,M_\odot$, with most lenses in the bulge. At a typical bulge $\pi_{\text{rel}} \sim 16\,\mu$as, the lenses at this peak mass would have $\pi_E \sim 0.07$, which is quite compatible with the parallax constraints. However, at a factor 2 below this peak, the parallax constraint $|\pi_{E,\parallel}| \lesssim 0.11$ starts to suppress many simulated events. Hence, the mass peak in Figure 13 is shifted higher relative to the Kim et al. (2021b) prediction.

5.5. KMT-2018-BLG-2602

As discussed in Section 3.6, we consider that its $\Delta\chi^2 = 10.3$ preference decisively resolves the degeneracy in favor of the outer solution. When we initially carried out the Bayesian analysis, we considered that there were only two constraints, one on $t_E = 99 \pm 14$ day (given by Table 6), and the other (from Tables 6 to 11) $\theta_E > 0.043$ mas. Moreover, as discussed in Section 3.6, the latter has almost no impact and is included only for completeness. In particular, we did not consider as relevant the fact that the lens must be fainter than the clump-giant blend. However, the resulting lens-distance histogram, which was qualitatively similar to the finally adopted one that is shown in Figure 13, contained a substantial fraction of nearby lenses that, at least potentially, might be excluded by even such a weak constraint. We therefore calibrated the pyDIA measured blend flux $[(V-I), I]_B = (2.99, 16.86)$ to obtain $I_L > 16.82$, and $V_L > 19.57$, using the same procedures as in Section 5.3. For this purpose, we used $A_I = 2.32$ from the KMT webpage, and $E(V-I) = A_I/1.10$, estimated from Figure 6 of Nataf et al. (2013). We find that these constraints have a small, but nonnegligible effect, as we quantify below.

The bimodal distance distribution, in Figure 13, can be understood as follows. For typical $\mu_{\text{rel}} \sim 6$ mas yr^{-1}, $\sqrt{\kappa M \pi_{\text{rel}}} = \theta_E = \mu_{\text{rel}} t_E \sim 1.7$ mas, which implies massive, nearby lenses, e.g., $M = 0.7\,M_\odot$, $D_L = 1.6$ kpc. Hence, a large number of simulated disk events are consistent with this timescale. On the other hand, the proper motions are, e.g., 5 times slower, so $\theta_E \sim 0.33$ mas would be consistent with massive lenses in the bulge. Such low proper motions are somewhat disfavored, but this is compensated by the high surface density of bulge stars compared to disk stars. Note, however, that, in both cases, relatively massive lenses are favored, as shown in the left panel.

As noted above, before including the lens-flux constraints, the Bayesian priors would favor large θ_E and hence massive, nearby lenses. Specifically, we find that this suppression of nearby disk lenses reduces the median value of M_{host} by 10% relative to the case of no flux constraint, while the median value of D_L is increased by 8%.

5.6. OGLE-2018-BLG-1119

For OGLE-2018-BLG-1119, there are two solutions. For each, there are three constraints: the first on t_E (as given in Table 7); the second on θ_E (as derived from Tables 7 and 11), i.e., $\theta_{E,\text{inner}} > 0.062$ mas, and $\theta_{E,\text{outer}} > 0.063$ mas; and the third on lens light $I_L > 19.7$ (as described in Section 4.6). We note that this limit is already on the OGLE-III calibrated scale.
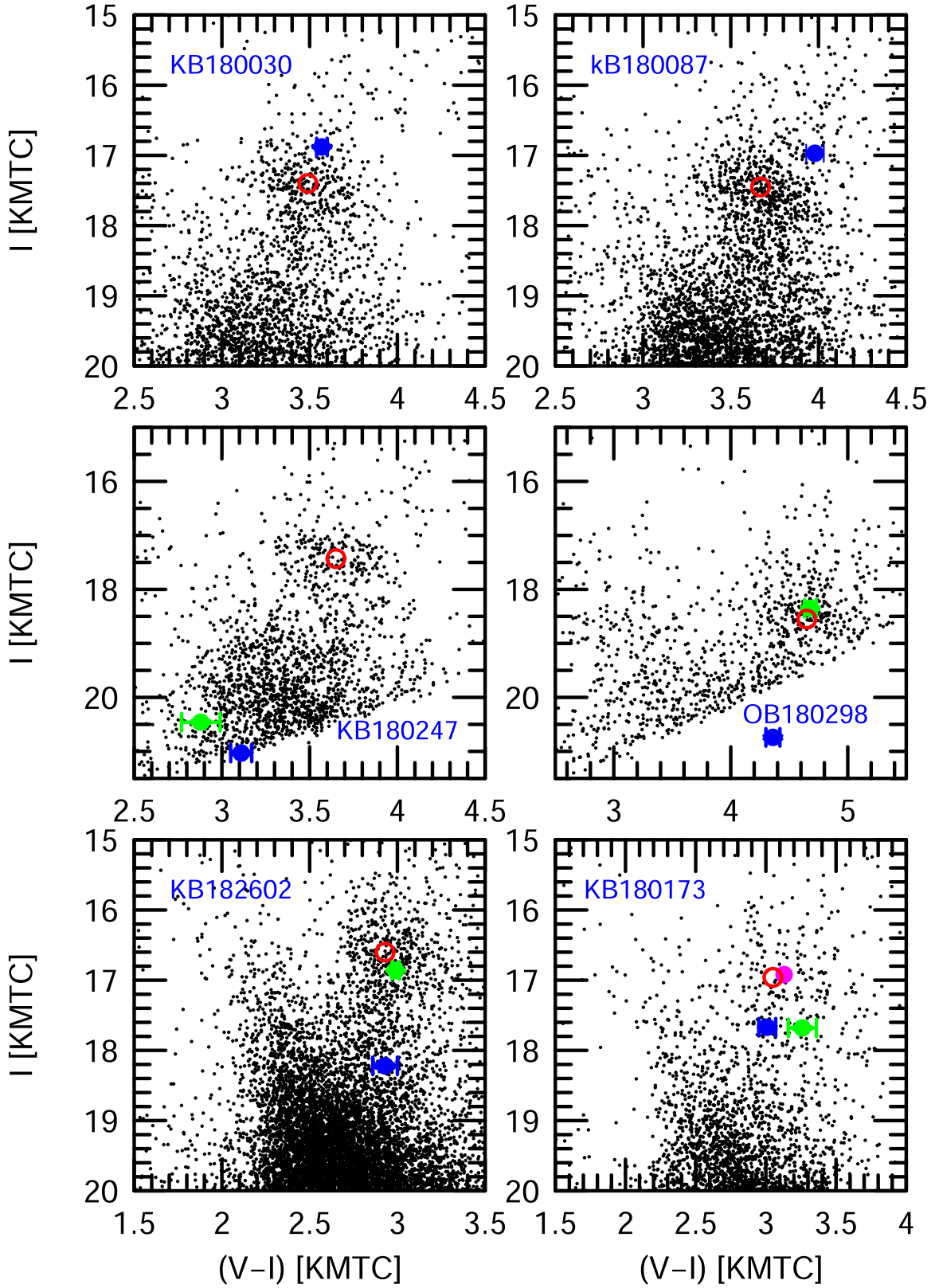
Figure 10. Color–magnitude diagrams for 6 of the events analyzed in this paper, each identified by an abbreviation, e.g., KB180030 for KMT-2018-BLG-0030. The centroid of the red clump and the lens position are always shown in red and blue, respectively. Where relevant, the blended light is shown in green. In one case (KB180173), we show the baseline object in magenta. When there are multiple solutions, we show only the source and blend for the lowest-χ^2 solution.

As in the case of KMT-2018-BLG-2602, the distance distribution is bimodal, and the explanation for this is similar: the event has a relatively long $t_{\rm E} \sim 40$ days, and there is only

an extremely weak constraint on $\theta_{\rm E}$. However, following the logic of Section 5.5 and noting that the timescale is significantly shorter than in that case, we expect the disk peak
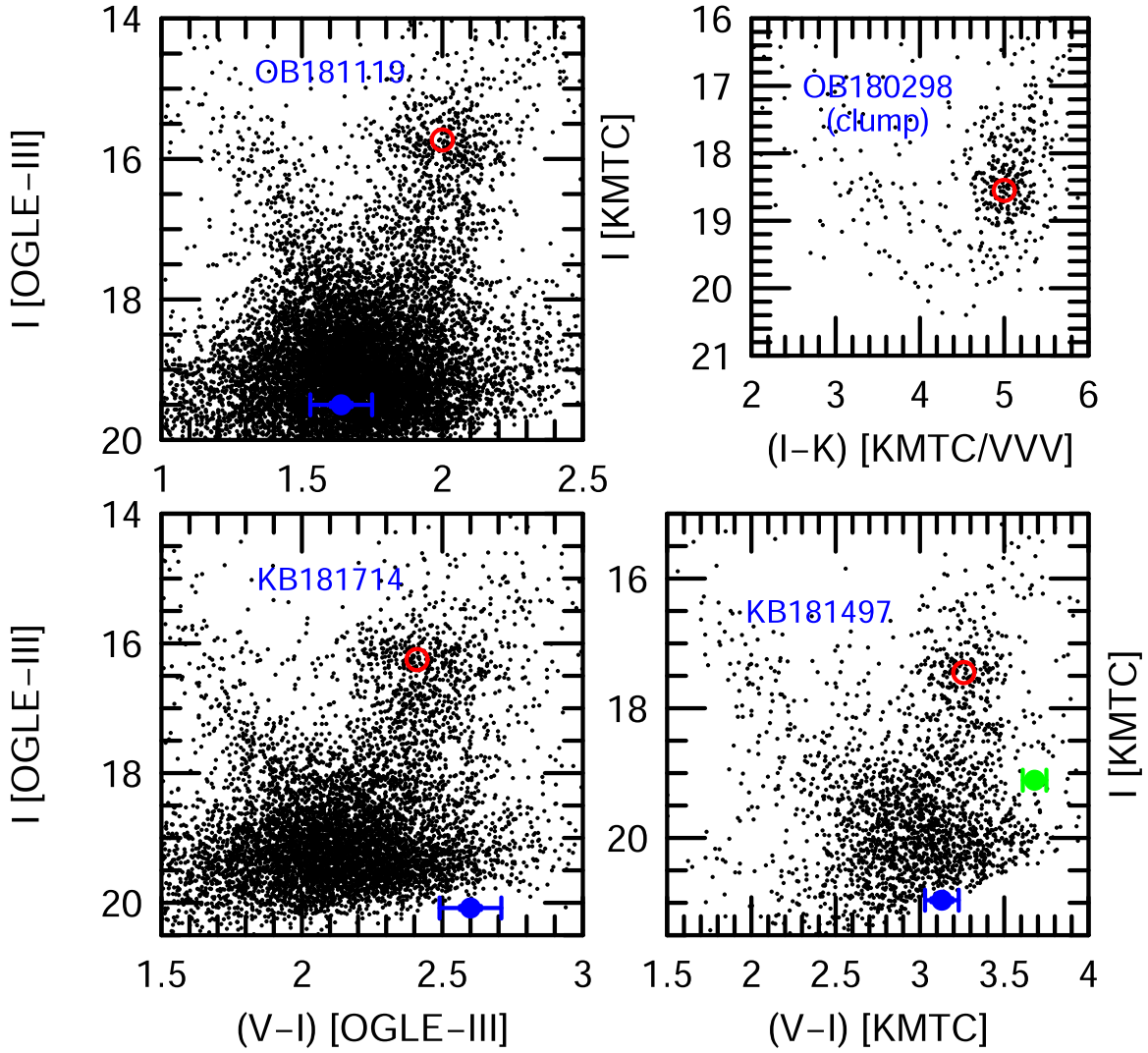
Figure 11. Same as Figure 10, but for the remaining 3 events (normal-sized panels). The undersized panel shows the determination of I_{cl} from an $[(I − K), I]$ CMD. See Section 4.4.

to be weaker, and the bulge peak to be stronger, while we expect the median mass to be significantly lower. All these expectations are confirmed by Figure 13 and Table 12.

6. Discussion

6.1. Summary of 2018 AnomalyFinder Detections

The main goal of this paper has been to complete the 2018 AnomalyFinder sample, with the ultimate purpose being to lay the basis for a mass-ratio function analysis. We summarize this work in Table 13, where we combine the results on the 9 planetary (or possibly planetary) events analyzed here with 10 previously published such events that were identified by the AnomalyFinder algorithm. We have divided these into 14 events that are likely to survive final selection for mass-ratio studies and 5 that are unlikely to survive. However, in this paper, we do not give final designations for individual events but, rather, provide the necessary information for others to do so. In Table 13, we indicate when there are multiple solutions and give the $(\log q, s)$ of the lowest-χ^2 solution. In future mass-ratio studies, it will be necessary to define a best-representative $\log q$ and to exclude events for which the different solutions are too divergent to do so.

We note that one previously published planetary event, KMT-2018-BLG-1996, was identified by the AnomalyFinder algorithm but was not selected in the by-eye review. This is one of only two such cases out of all previously published planets from 2016 to 2019 that were recovered by the AnomalyFinder algorithm. Because the number of such failures is small, they do not generate a significant systematic effect. We therefore believe that this event should be included in the mass-ratio function sample. Again, however, it is not the purpose of this paper to make a final decision on this issue.

Table 13 should be compared to Table 14 of Gould et al. (2022), which contains a total of 26 planetary (or possibly planetary) events. Three of those events (below the line) are clearly unsuitable for mass-ratio studies. In addition, as noted by Gould et al. (2022), the OGLE-2018-BLG-1700 planet was discovered in a binary system, which makes it subject to different selection biases. Further, the 1L2S–2L1S degeneracy of OGLE-2018-BLG-1544 is likely to be too severe to include it, while the mass-ratio uncertainties of KMT-2018-BLG-1025 and OGLE-2018-BLG-1126 are too severe to include them. Hence, it is plausible that a total of approximately 33 (14 sub-prime-field and 19 prime-field planets) will be available from

Table 12
Physical Properties

Event	Physical Parameters				Relative Weights	
Models	M_{host} ($M_\odot$)	M_{planet} (M_{Jup})	D_L (kpc)	$a_\perp$ (au)	Galactic Modulus	χ^2
KB180030	$0.51^{+0.43}_{-0.31}$	$1.45^{+1.23}_{-0.88}$	$6.48^{+1.28}_{-1.96}$	$4.39^{+2.18}_{-2.40}$	1.00	1.00
KB180087						
Inner	$0.11^{+0.15}_{-0.06}$	$0.32^{+0.43}_{-0.16}$	$6.90^{+1.04}_{-1.16}$	$0.66^{+0.20}_{-0.21}$	0.62	0.07
Outer	$0.10^{+0.14}_{-0.05}$	$0.23^{+0.32}_{-0.12}$	$7.02^{+1.03}_{-1.15}$	$0.87^{+0.24}_{-0.25}$	1.00	1.00
Adopted	$0.10^{+0.14}_{-0.05}$	$0.23^{+0.32}_{-0.12}$	$7.02^{+1.03}_{-1.15}$	$0.87^{+0.24}_{-0.25}$		
KB180247						
Close	$0.35^{+0.31}_{-0.18}$	$2.33^{+2.07}_{-1.18}$	$6.47^{+0.99}_{-1.33}$	$2.11^{+0.43}_{-0.52}$	0.65	0.44
Wide	$0.27^{+0.28}_{-0.14}$	$2.04^{+2.09}_{-1.04}$	$6.84^{+0.99}_{-1.24}$	$2.56^{+0.51}_{-0.58}$	1.00	1.00
Adopted	$0.29^{+0.28}_{-0.14}$	$2.11^{+2.09}_{-1.04}$	$6.76^{+0.99}_{-1.24}$	$2.46^{+0.51}_{-0.58}$		
OB180298						
Close	$0.70^{+0.34}_{-0.30}$	$0.15^{+0.07}_{-0.06}$	$6.49^{+0.95}_{-1.23}$	$2.84^{+0.73}_{-0.80}$	1.00	1.00
Wide	$0.63^{+0.34}_{-0.27}$	$0.091^{+0.049}_{-0.038}$	$6.79^{+0.89}_{-1.07}$	$2.98^{+0.54}_{-0.59}$	0.91	0.27
Adopted	$0.69^{+0.34}_{-0.30}$	$0.14^{+0.07}_{-0.06}$	$6.54^{+0.95}_{-1.23}$	$2.86^{+0.73}_{-0.80}$		
KB182602	$0.66^{+0.42}_{-0.36}$	$1.15^{+0.73}_{-0.63}$	$4.31^{+1.97}_{-1.84}$	$3.81^{+2.96}_{-2.32}$	1.00	1.00
OB181119						
Inner	$0.48^{+0.35}_{-0.28}$	$0.91^{+0.66}_{-0.52}$	$5.76^{+1.43}_{-2.48}$	$4.11^{+2.14}_{-2.58}$	1.00	1.00
Outer	$0.48^{+0.35}_{-0.28}$	$0.86^{+0.62}_{-0.49}$	$5.70^{+1.47}_{-2.48}$	$3.13^{+1.65}_{-1.98}$	0.89	0.06
Adopted	$0.48^{+0.35}_{-0.28}$	$0.91^{+0.66}_{-0.52}$	$5.76^{+1.43}_{-2.48}$	$4.06^{+2.14}_{-2.58}$		

2018 alone for mass-ratio studies. This would be the largest microlensing planet sample to date.

6.2. 6D Distribution

In Figure 14, we show a six-dimensional (6D) representation of these 33 planets, including 2 continuous dimensions (given by the axes) and 4 discrete dimensions that are represented by colors and point types. The abscissa and ordinate are $\log q$ and $I_{S,anom} \equiv I_S - 2.5 \log[A(u_{anom})]$, with the latter being the source brightness in the unperturbed event at the time of the anomaly. The planets from the prime fields are marked in primary colors (red and blue), while the planets from the subprime fields are marked in nonprimary colors (orange and cyan). The planets that were discovered by AnomalyFinder are marked in reddish colors (red and orange), while those previously identified by eye are marked in bluish colors (blue and cyan). The planets with major-image anomalies are shown as triangles, those with minor-image anomalies are shown as circles, while the two that cannot be classified as either (KMT-2018-BLG-0247 and OGLE-2018-BLG-0740) are shown as squares. The events for which the source crossed a caustic are shown as filled symbols, while those for which it did not are shown as open symbols.

The most striking feature of this diagram is the apparent threshold of AnomalyFinder detection at $I_{S,anom} = 18.75$, with one major exception (OGLE-2018-BLG-0962) and one minor exception (KMT-2018-BLG-2718), both being relatively high-q planets. Another very striking feature is the paucity of by-eye detections of non-caustic-crossing events (open bluish symbols) at low q: 1 (OGLE-2018-BLG-1185) out of 5 for $\log q < -3$ compared to 7 out of 12 for $\log q > -3$. It is also notable that among the 16 caustic-crossing events, all but two were discovered by eye. Moreover, both of the AnomalyFinder discoveries (OGLE-2018-BLG-0383 and OGLE-2018-BLG-0977) were in prime fields, and at $\log q < -3$, a regime where

machines may do better than people because the relatively weak signals of low-q events are spread out over a greater number of data points. That is, it appears that AnomalyFinder was essential to finding low-q events, both with and without caustic crossings.

Zhu et al. (2014) predicted that roughly half of all planet detections in a KMT-like survey would not have caustic-crossing features. The 2018 AnomalyFinder sample, which has 16 caustic-crossing and 17 non-caustic-crossing events, is consistent with this prediction.

Another anticipated feature of the KMT survey is also confirmed. When KMT began regular observations in 2016, it adopted the layered approach pioneered by OGLE, in which a relatively small region would be monitored at high cadence (which we call the "prime fields"), and much larger regions would be monitored at a series of lower cadences (Kim et al. 2018a). It was expected that the higher-cadence fields would be more sensitive to lower-q planets (Henderson et al. 2014). Figure 14 shows that, for $\log q < -3$, 9 of 11 planets are from prime fields (primary colors), compared to 10 out of 22 for $\log q > -3$.

Finally, there are 14 planets with major-image perturbations, compared to 17 with minor-image perturbations, which is statistically consistent with the expectation that these should be about equal.

6.3. Role of Gaia in Planetary Microlensing

The 2018 AnomalyFinder statistical sample, which the present work has completed, provides an excellent opportunity to systematically investigate the role of Gaia astrometry in planetary microlensing. First, with 33 planets, it is larger than any of the three previous statistical samples, i.e., the Gould et al. (2010) 6-planet sample from Microlensing Follow Up Network (μFUN) observations of high-magnification events that were discovered by OGLE and MOA over 4 yr
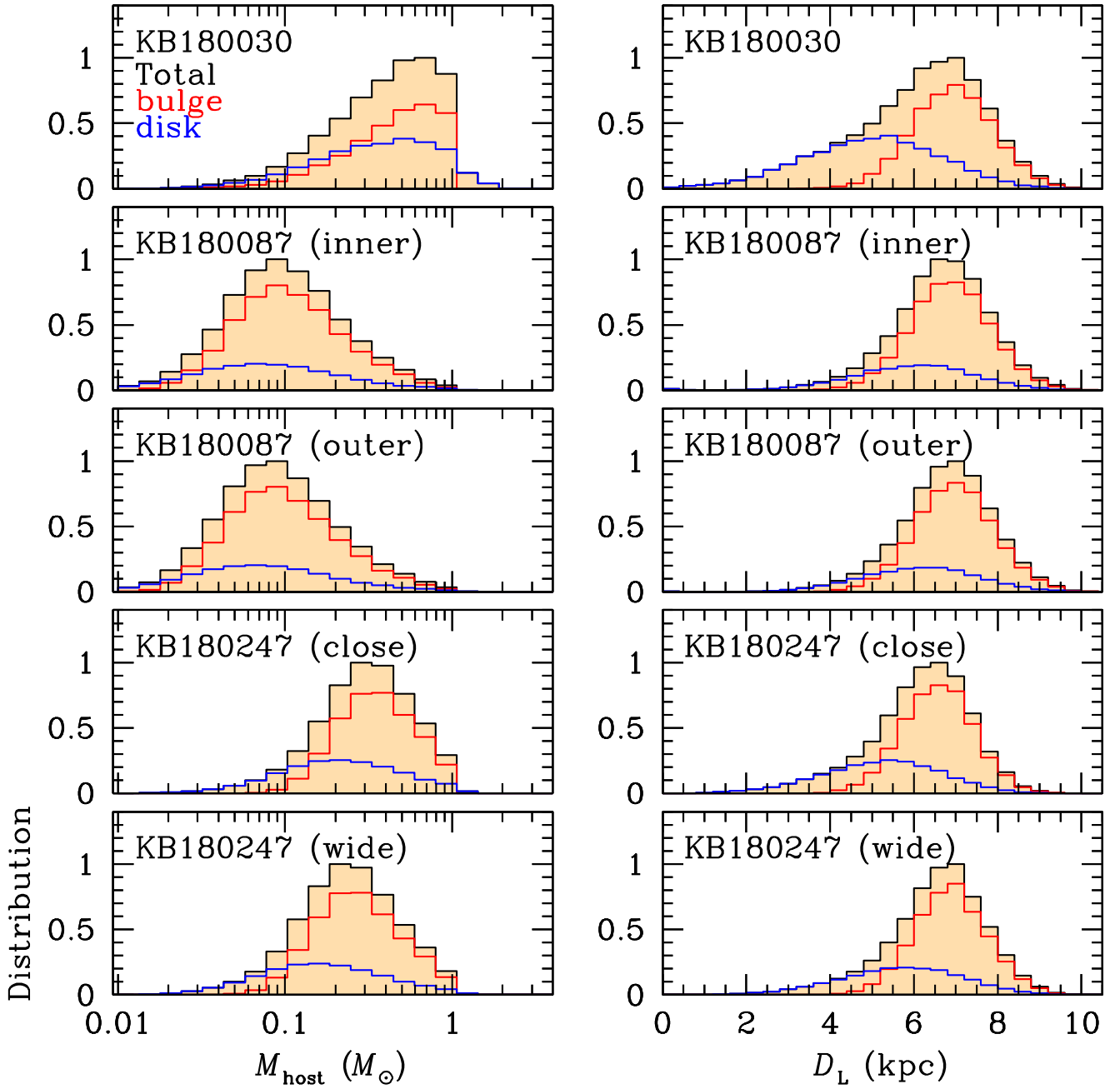
Figure 12. Histograms of the host mass (left) and lens distance (right) for 3 of the 6 unambiguously planetary events, as derived from the Bayesian analysis. Disk (blue) and bulge (red) distributions are shown separately, with their total shown in black.

(2005–2008), the Shvartzvald et al. (2016) 8-planet sample based on essentially continuous observations by OGLE, MOA, and Wide-field Infrared Survey Explorer of 8 deg^2 over 4 yr (2011–2014), and the 22-planet Suzuki et al. (2016) sample based on MOA observations over 6 yr (2007–2012). Equally important, however, it is the first statistical survey for which all of the planets have been analyzed during the Gaia era. This means that we can ask not only how Gaia data can in principle be used but also how they actually have been used.

Gaia data are potentially useful if they can, directly or indirectly, characterize the lens system, i.e., directly, by measuring the parallax and proper motion (PPM) of the lens (or possibly its binary companion), or indirectly, by measuring the proper motion of the source. For the latter case, i.e., indirect constraints, there must be some additional information about

lens–source relative proper motion, μ_{rel}, in order to constrain the properties of the lens by measurements of the source. In principle, individual-epoch Gaia astrometry could also be used to measure θ_{E} (Miyamoto & Yoshii 1995; Hog et al. 1995; Walker 1995). However, a proper investigation of this possibility must await the release of such data.

Thus, for the Gaia data to be useful at all, the Gaia entry must be strongly dominated by either the source or the lens (or both). In principle, it can be dominated by binary companions to either of these objects, but great care is usually required to make such identifications. In particular, both OGLE and KMT photometry are both deeper and of higher resolution than Gaia, so Gaia data cannot further clarify issues of blending and source confusion.
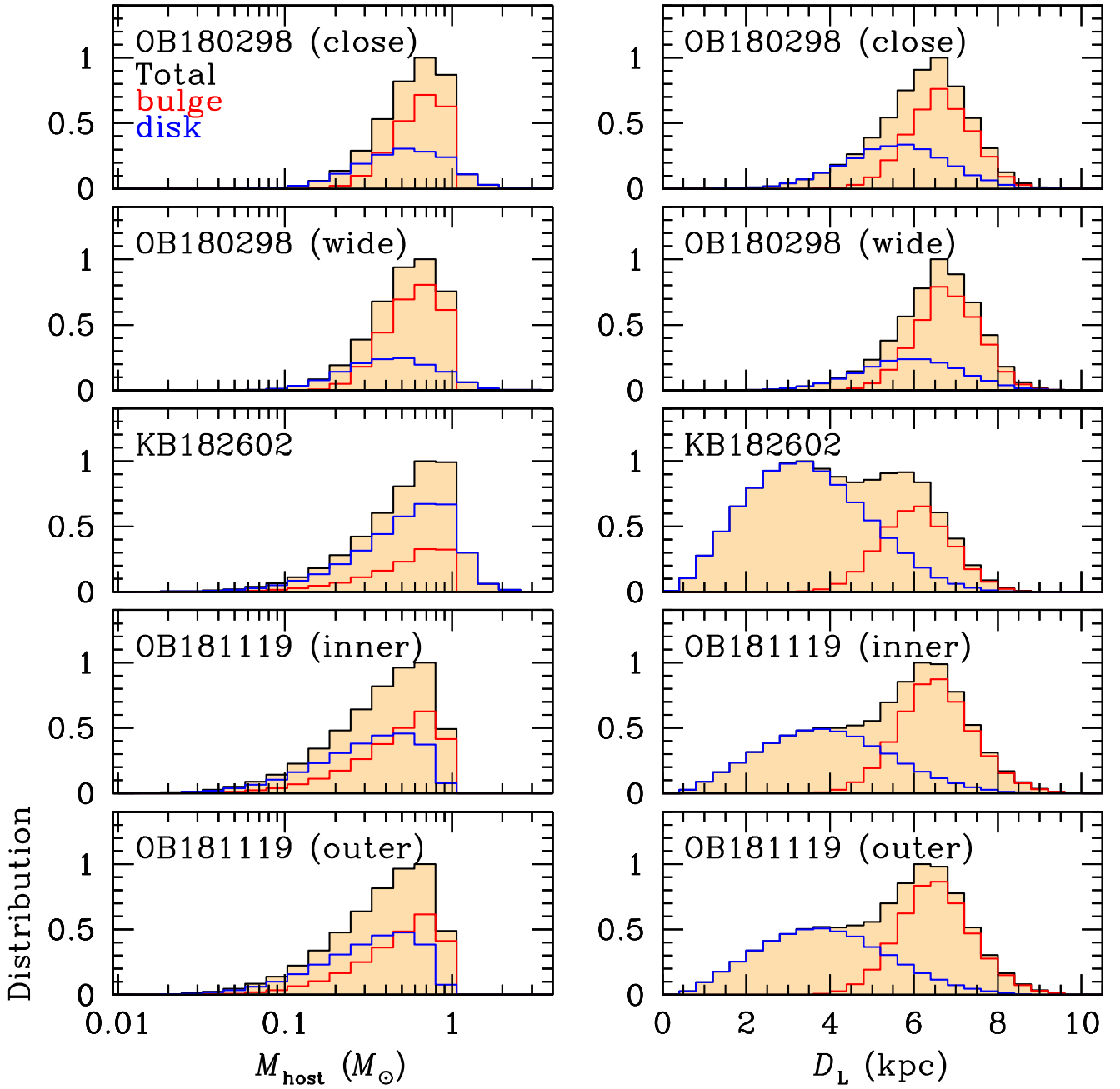
Figure 13. Same as Figure 12, except that this figure shows the remaining 3 unambiguously planetary events.

Nevertheless, in order to develop a comprehensive understanding of the role of Gaia, we do not initially focus narrowly on finding cases for which the Gaia entry can be identified with the source and/or the lens, but rather begin by considering all planetary events in the sample.

We therefore start by finding the closest Gaia entry to the published event coordinates of each of the 32 events (with 33 planets). The results are presented in Table 14 and illustrated in Figure 15. The first two columns of Table 14 give the event name and the source magnitude I_S taken from the best model. The next three columns give the offset (radius, east, and north) of the Gaia entry relative to the tabulated source position. The next six columns give the Gaia parallax, proper motion (east and north), and their errors. The last three columns give the Gaia RUWE indicator, magnitude, and color, i.e., G and

$B_p - R_p$. For offsets $\Delta\theta > 0''.5$, only the positions are shown because the Gaia entry is almost certainly unrelated to the event. The events are ordered by I_S, with the general expectation that brighter sources will have more Gaia information. One can see immediately that this expectation is only partially confirmed, and the discrepancies provide useful entry points into the investigation.

Figure 15 shows the vector offsets for the 32 events. The colors reflect the source magnitudes, i.e., black, red, green, cyan, blue, magenta, as indicated in the legend. With four exceptions (see below), Gaia entries that have $\Delta\theta < 0''.5$ and 5-parameter (PPM) solutions are shown as filled circles, while those with only the position measurements are shown as open circles. The four exceptions are the cases for which the Gaia entry is dominated by a star other than the source, which is

Table 13
AnomalyFinder Planets in KMT Subprime Fields for 2018

Event Name	KMT Name	$\log q$	s	Reference
KB180029	KB180029	−4.74	1.00	Gould et al. (2020)
OB180298[AA]	KB181354	−3.71	0.96	This Work
KB181996[DD]	KB181996	−2.82	1.46	Han et al. (2021a)
KB182602	KB182602	−2.78	1.18	This Work
OB181428	KB180423	−2.76	1.42	Kim et al. (2021a)
OB181119[AA]	KB181870	−2.74	0.64	This Work
KB180087[AA]	KB180087	−2.67	2.17	This Work
OB180799	KB181741	−2.60	1.13	Zang et al. (2022a)
KB180030	KB180030	−2.56	1.58	This Work
KB181976[AA]	KB181976	−2.50	1.23	Han et al. (2021a)
KB181292	KB181292	−2.45	1.36	Ryu et al. (2020)
KB181990 [AA,BB]	KB181990	−2.45	0.96	Ryu et al. (2019)
OB180740[AA]	KB181822	−2.34	1.26	Han et al. (2019)
KB180247[AA]	KB180247	−2.15	1.12	This Work
KB181988 [AA,GG]	KB181988	−4.45	1.04	Han et al. (2021c)
KB181497 [AA,CC,GG]	KB181497	−3.68	1.13	This Work
KB180173 [AA,CC]	KB180173	−2.98	0.48	This Work
KB181743 [AA,GG]	KB181743	−2.92	1.05	Han et al. (2021b)
KB181714 [AA,CC,GG]	KB181714	−2.43	0.92	This Work

Note. Event names are abbreviations for, e.g., KMT-2018-BLG-0029 and OGLE-2018-BLG-0799. s degeneracy (AA). Factor 1.6 q degeneracy (BB). 1L2S–2L1S degeneracy (CC). Not selected in AnomalyFinder review (DD). Large q degeneracy (GG).

nevertheless seen in very close projection ($\Delta\theta < 0''.2$) to it, i.e., inside the yellow circle.

6.3.1. $\Delta\theta > 0''.5$

The 10 Gaia entries with $\Delta\theta > 0''.5$ are shown as crosses. In fact, all 10 have $\Delta\theta > 0''.85$. The first point to note about these is that seven of the 10 have $I_S > 19.5$ (blue and magenta), for which we expect very few Gaia counterparts. Indeed, there are only 5 such faint stars with matches to Gaia, three of which are *stars* (i.e., the Gaia entry is not dominated by the source), and the other two of which lack PPM. Furthermore, two of the remaining three stars have $19.0 < I_S < 19.5$, compared to only one (out of five others) that has a PPM measurement of the source (see below). In brief, Gaia contains very little astrometric information for sources $I_S > 19.0$. This may change over time as future data releases report results from additional years of data, which could *update* some of the open circles to filled circles.

6.3.2. $0''.2 < \Delta\theta < 0''.5$

We next examine the distinct group of four events with $0''.2 < \Delta\theta < 0''.5$. In all four cases, the Gaia and KMT source positions are correctly matched, and the relatively large offsets are due to known causes.

As we now show, in the first case, OGLE-2018-BLG-1119, the large offset is due to source confusion. In Section 4.6, we noted that there are two stars that both OGLE and KMT find to be separated by $\sim 0''.8$ but with very different distributions of the light. By contrast, the nearest neighbor found by Gaia lies $\sim 1''.7$ to the east. As this star is also found by OGLE-III, we can conclude either that the Gaia entry is a blend of the two OGLE-III stars that are nearest to the source or at least that the Gaia astrometry is corrupted by the nearby neighbor that
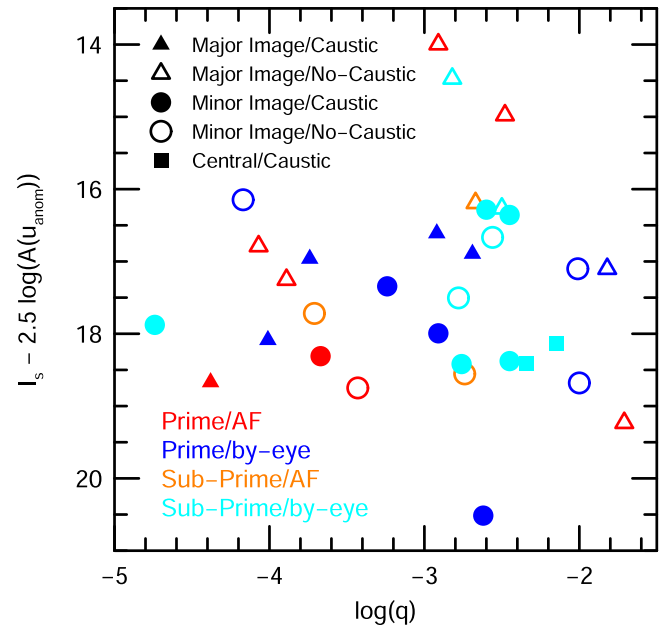

Figure 14. Six-dimensional scatter plot of 33 planets. (1) Abscissa: log mass ratio. (2) Ordinate: source magnitude of unperturbed event at time of anomaly. (3) Primary (red, blue) vs. nonprimary (orange, cyan) colors; prime vs. subprime fields. (4) Reddish (red, orange) vs. bluish (blue, cyan) colors; AnomalyFinder vs. by-eye discoveries. (5) Filled vs. open symbols: caustic-crossing vs. non-caustic-crossing anomalies. (6) Shape: major-image (triangles), minor-image (circles), and central-caustic (squares) perturbations. The two most important patterns are: (A) a threshold of detections at $I_S − 2.5\log[A(u_{anom})] = 18.75$, and (B) the dearth of by-eye discoveries of non-caustic-crossing anomalies (bluish open symbols) for $\log q < −3$.

OGLE-III detects at $0''.8$ to the west, but Gaia does not. As there is no PPM solution for this entry, the existence of a Gaia counterpart is of little immediate interest. Moreover, this also means that there is no RUWE parameter, which would give an indication of Gaia reduction difficulties. Hence, all we say at the present time is that Gaia does not provide useful information for this event.

We now examine the remaining three of these four events (KMT-2018-BLG-1990/1996/2602), for all of which the KMT positions come from an internal DoPhot (Schechter et al. 1993) catalog, which has substantially lower precision than the external catalogs (OGLE-III; Szymański et al. 2011; DECam; Schlafly et al. 2018) that cover most of the KMT survey area. See Figure 1 from Kim et al. (2018b). As noted in Section 4.5, for KMT-2018-BLG-2602, the blended light is within 10 mas of the source on the internal pyDIA system. Therefore, as also noted in that section, the Gaia entry represents the combined light from the source and a several times brighter blend, which is very likely its companion. Nevertheless, because there is no information about μ_{rel} for this event, the Gaia measurement cannot significantly constrain the lens properties. The source of KMT-2018-BLG-1996 is relatively bright, and therefore, the Gaia proper motion can be taken at face value. Han et al. (2021a) did not make use of this measured μ_S. However, because μ_S is that of a typical bulge star, while the light curve does not yield a μ_{rel} measurement, incorporating the μ_S measurement would not have significantly affected their Bayesian analysis.

Ryu et al. (2019) reported that they did not find a Gaia counterpart in data release 2 (DR2) for KMT-2018-BLG-1990. In fact, DR2 has a star at the same location as data release 3

Table 14
Gaia Data for 32 AnomalyFinder Events of 2018

Event	I_S	$\Delta\theta$	$\Delta\theta_E$	$\Delta\theta_N$	π	σ	μ_E	σ	μ_N	σ	RUWE	G	$B-R$
OB180932	16.79	0.13	−0.11	−0.08	+0.60	0.24	−8.81	0.26	−7.53	0.18	1.25	18.36	
KB180030	16.88	0.18	−0.01	+0.18	+0.26	0.57	−10.92	0.66	−7.79	0.44	2.15	18.43	3.36
KB180087	16.97	0.04	+0.00	+0.04								20.37	
OB180596	17.19	0.02	−0.01	+0.01	+0.97	0.24	−4.66	0.26	−4.58	0.16	1.07	18.62	2.50
OB180799	17.25	0.18	−0.12	−0.13	−0.27	0.46	−2.40	0.37	−5.90	0.30	1.75	18.56	1.93
OB180567	18.20	0.12	−0.08	−0.09	+0.33	0.31	−3.96	0.38	−8.01	0.23	1.07	18.96	3.51
KB182602	18.22	0.38	−0.06	+0.36	+0.12	0.14	−2.37	0.19	−9.89	0.12	0.99	17.96	2.82
KB181976	18.24	0.05	+0.04	−0.03	+0.14	0.78	+0.63	0.86	−11.70	0.46	2.03	19.51	
OB180383	18.37	0.13	−0.05	−0.12	−0.15	0.14	+1.04	0.12	−8.06	0.08	0.93	17.04	2.52
OB181212	18.52	0.17	+0.06	−0.16	+3.41	0.93	−7.32	1.15	−4.73	0.98	1.89	19.36	
KB181996	18.82	0.45	−0.43	+0.10	−1.05	1.24	−1.94	1.14	−7.86	0.77	1.14	20.28	2.85
OB181367	18.94	1.71	−1.67	−0.37									
OB181428	18.97	0.14	−0.05	−0.13	−1.13	0.96	+0.38	1.21	−5.28	0.66	1.15	20.43	2.48
KB181292	19.08	0.05	−0.05	+0.00	+0.05	0.36	+1.95	0.45	−2.04	0.30	1.06	19.32	
KB180748	19.21	1.82	−0.35	+1.79									
KB181990	19.36	0.49	−0.31	+0.38	−3.56	1.71	−4.78	2.07	−10.79	1.39	1.74	20.50	
OB180506	19.37	0.09	+0.05	−0.07								20.75	2.35
OB181269	19.42	0.07	−0.06	+0.04	+0.27	0.13	−1.26	0.14	−0.97	0.10	1.51	17.17	1.83
OB180516	19.45	0.11	−0.10	−0.02								20.66	
KB182004	19.48	1.89	−1.12	−1.52									
OB181119	19.50	0.31	−0.31	−0.06								20.10	
OB181011	19.93	0.10	−0.07	+0.07								19.92	
OB181185	20.11	0.18	−0.16	−0.08	−1.20	1.24	−12.17	1.25	−9.71	0.87	1.03	20.10	1.84
OB180977	20.20	2.70	−0.97	−2.52									
OB180298	20.74	0.12	−0.16	−0.11	−0.48	0.98	−0.60	1.47	−6.97	0.79	1.07	19.88	3.21
OB181647	20.87	1.52	+1.44	+0.50									
KB180247	21.03	2.42	−1.18	+2.10									
OB180962	21.40	1.29	−0.44	+1.22									
OB180740	21.54	0.19	+0.01	−0.19	+0.96	0.14	+2.05	0.15	−5.24	0.11	1.15	17.72	1.67
KB180029	21.84	0.83	+0.69	−0.47									
OB180532	22.23	1.36	+0.99	−0.93									
KB182718	22.60	1.85	−0.15	−1.84									

Note. Event names are abbreviations for, e.g., KMT-2018-BLG-0029 and OGLE-2018-BLG-0799. Units of θ, π, and μ, are arcseconds, milliarcseconds, and milliarcseconds per year, respectively.

(DR3) but without a PPM solution, so either Ryu et al. (2019) considered $\Delta\theta \simeq 0''.5$ to be too far for a good match, or they considered that the lack of a PPM solution implied no useful information, or both. However, we now understand that the large offset is consistent with the general behavior of KMT DoPhot catalog stars. Ryu et al. (2019) found that the baseline-object *I*-band light is split almost equally between the source and another star that is bluer by $\Delta(V-I) = 0.20$ mag. They did not measure the offset between the source and the baseline object, but we find $\Delta\theta = 90$ mas, implying an offset between the two stars of 180 mas. Hence, the blend cannot be the lens, and its position on the CMD makes it very unlikely to be a companion to the source. The chance of a random interloper within this separation is about 1%, meaning that the blend could be a companion to the lens. However, there is no compelling evidence that this is the case. Hence, the Gaia entry is a mixture of the source and another star of unknown provenance. Probably as a reflection of this, it has a high RUWE = 1.7 value. Therefore, the Gaia proper motion cannot be used.

In brief, two of these four outliers on the offset diagram cannot be used because the Gaia entry is a poorly understood blend, while the other two have limited value because there is no information about μ_{rel}.

6.3.3. $\Delta\theta < 0''.2$

We now turn to the 18 events that lie inside the yellow circle, beginning with the four events (*stars*) for which the source does not dominate the Gaia entry.

Han et al. (2019) noted that the Gaia entry for OGLE-2018-BLG-0740 was completely dominated by light from the lens. They therefore adopted the Gaia measurement as the proper motion of the lens, μ_L. They used DR2, but DR3 is consistent with DR2 at slightly more than 1σ, so their conclusions would not be affected by this update. There is one curious point, however: Han et al. (2019) obtained a spectrum of the lens, which (when combined with the light-curve solution) implied a lens distance of $D_L = 3.2 \pm 0.5$ kpc, i.e., $\pi_L = 0.32 \pm 0.05$ mas. This would be quite consistent with the DR2 parallax measurement, $\pi = 0.27 \pm 0.19$ mas, but would be in nominal conflict with the DR3 measurement, $\pi = 0.96 \pm 0.14$ mas. Most likely, this discrepancy can be accounted for by the fact that Gaia astrometric errors are underestimated in the crowded fields of the bulge (Rybizki et al. 2022).

Similarly, Jung et al. (2020a) noted that the Gaia entry for OGLE-2018-BLG-1269 was strongly dominated by light from the lens, and they also adopted the Gaia proper motion to be that of the lens, μ_L. They also used DR2. Combining this with photometry of the lens and microlensing measurements of θ_E
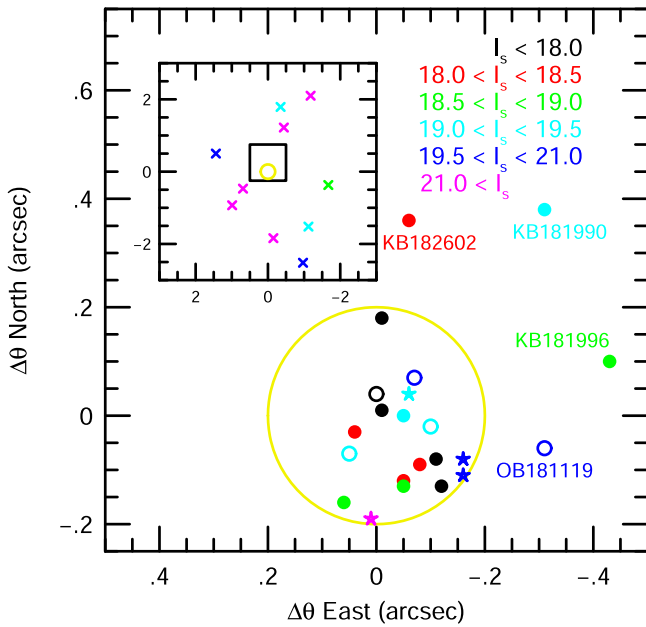
Figure 15. Astrometric offsets $\Delta\theta$ of nearest Gaia entry relative to KMT coordinates for 32 events (33 planets) likely to form the 2018 statistical sample. There are 18 excellent matches (yellow circle), four other real matches in the main panel, and 10 spurious matches to unrelated stars (inset, crosses). Filled circles have full PPM Gaia solutions, while open circles only have Gaia positions. Events for which the baseline object is dominated by a star other than the source are shown as star symbols. Events are color-coded by source magnitude (see legend).

and $\pi_{E,\parallel}$, they derived a lens distance of $D_L = 2.6^{+0.9}_{-0.6}$ kpc, which they noted was compatible with Gaia parallax $\pi = 0.73 \pm 0.18$ mas (which they adjusted to $\pi = 0.78 \pm 0.18$ mas for the zero-point error). We find that the DR3 proper motion changes very little. The DR3 parallax (after the same adjustment) would be $\pi = 0.32 \pm 0.13$ mas, which is even more compatible with their distance estimate.

Regarding OGLE-2018-BLG-1185, Kondo et al. (2021) showed that the blend star, which dominates the light of both the Gaia entry and the OGLE-III catalog star, is separated from the source by 175 mas and is unrelated to the event. Note that they also found that the Gaia proper motion of this blend star (which has a highly unusual value) strongly conflicts with the OGLE-based proper motion (which has a very typical value), and they therefore concluded that the Gaia proper motion was spurious. As discussed in Section 4.4, the blend star for OGLE-2018-BLG-0298, which dominates the light of both the Gaia entry and the DECam (Schlafly et al. 2018) catalog star, is separated from the source by 400 mas and is unrelated to the event.

In brief, in two of these four cases for which *another star* dominates the light of the Gaia entry, the *other star* is the lens, and so Gaia contributes critically important information. In the other two cases, the Gaia entry is unrelated to the event.

Of the remaining 14 events inside the yellow circle, four (KMT-2018-BLG-0087, OGLE-2018-BLG-0506, OGLE-2018-BLG-0516, and OGLE-2018-BLG-1011) lack PPM solutions, and therefore Gaia data do not contribute to our understanding of these events. However, it is possible that there will be PPM solutions in future Gaia updates.

Finally, we review the 10 remaining stars, all of which have PPM solutions.

KMT-2018-BLG-0030 is the only planetary event for which we presented an analysis in the current paper that has a source proper-motion measurement from Gaia. In Section 4.1, we expressed skepticism about this measurement; in part because, if correct, the source would be a 2.9σ outlier relative to bulge stars; and in part because, its large RUWE value signals some sort of internal problem with the Gaia reductions. Hence, we did not incorporate this measurement into the Bayesian analysis. The current investigation provides an additional reason for caution in that KMT-2018-BLG-0030 appears to be an outlier among the *good matches* inside the yellow circle in Figure 15. If we eliminate this object and also KMT-2018-BLG-0087 (see below), then the remaining 16 stars have Gaia-KMT offsets (mean and standard deviation) of

$$\langle \theta(E, N) \rangle = (-54 \pm 67, -68 \pm 71)\,\text{mas}$$
$$(Gaia - \text{KMT}). \tag{17}$$

Hence, the standard errors of the mean in the two directions are (17, 16) mas, implying that the offset is detected at 4.9σ. The physical cause of this offset is that the Gaia and KMT catalogs are calibrated at different epochs. For 9 of these 16 stars, KMT astrometry derives from OGLE-III, which has a mean epoch of 2006. Hence, assuming that the great majority of the stars are in the bulge, they moved on average $\langle \Delta\theta(E, N) \rangle = (-30 \pm 29, -52 \pm 29)$ mas by the Gaia epoch. The other 9 stars within the yellow circle are derived from DECam (Schlafly et al. 2018). According to their Figure 12, 7 of these 9 were calibrated to Two Micron All Sky Survey, which implies a $\sim$1.5 times longer baseline, and so $\langle \Delta\theta(E, N) \rangle = (-45 \pm 43, -76 \pm 29)$ mas. Combining these two gives $\langle \Delta\theta(E, N) \rangle = (-37 \pm 35, -63 \pm 35)$ mas, whose means are very similar to Equation (17). Of course, the observed scatter in Equation (17) is larger than the theoretical prediction based on the bulge proper-motion dispersion. This is partly due to the measurement error, but also partly due to discretization errors of (37, 25) mas. This means that the scatter induced by measurement error (including discretization noise) is $\sim\sqrt{69^2 - 35^2} = 57$ mas.

According to Figure 12 from Schlafly et al. (2018), the remaining two stars were calibrated to Gaia and so should have zero expected offset. This is actually true of KMT-2018-BLG-0087. However, KMT-2018-BLG-0030 has an offset of 180 mas, i.e., 3.2σ. Thus, KMT-2018-BLG-0030 is a significant outlier in three respects, large proper motion relative to the bulge mean, large RUWE parameter, and large positional offset. Hence, the Gaia measurement should not be relied upon to characterize the planetary event.

Motivated by the previous example, we next examine the three other events (KMT-2018-BLG-1976, OGLE-2018-BLG-1212, and OGLE-2018-BLG-0799) that have high RUWE (2.03, 1.89, and 1.75) to determine whether they, like KMT-2018-BLG-0030, also exhibit independent causes for concern.

KMT-2018-BLG-1976 has low blending, consistent with zero. However, the light-curve analysis did not yield any information about $\mu_{\rm rel}$, i.e., neither measurements of $\mu_{\rm rel}$ nor π_E. Therefore, incorporating the Gaia measurement of μ_S would not be constraining, and Han et al. (2021a) did not do so. We note that, in Galactic coordinates, $\mu_S(l, b) \simeq (-9.8, -6.4)$ mas yr^{-1}, which is about 2.6σ from the mean of the bulge distribution. This should be regarded as a reason for moderate

concern. That is, certainly such stars exist, but they are rare, and this one has already been flagged for high RUWE.

Gould et al. (2022) comment extensively on the case of OGLE-2018-BLG-1212 because there is strong independent evidence that the lens is nearby, while the Gaia parallax is high, $\pi = 3.41 \pm 0.93$ mas, and the blend-to-source flux ratio is fairly high, $f_S/f_B = 0.60$. Thus, they considered the possibility that a very nearby lens contributes the blended light, thereby driving up the parallax. However, they showed that this cannot be the case for the lens itself and that it is also very unlikely that the blend is due to a companion to the lens. Hence, they regarded the Gaia measurement as suspect and did not include it in their Bayesian analysis. However, we note here that, while the parallax measurement is very unusual, the proper-motion measurement, $\mu(l, b) \simeq (-7.8, +4.0)$ mas yr^{-1}, is not. Nevertheless, it is again striking that this high RUWE star has a $\sim 3.7\sigma$ parallax *detection* that is almost certainly incorrect.

OGLE-2018-BLG-0799 is a very complex case in which a wrong Gaia measurement of μ_S contributed significant confusion to the analysis of the event. When Zang et al. (2022a) originally submitted their manuscript in 2020, they incorporated the DR2 measurement $\mu_S(E, N) = (+0.54 \pm 0.74, -6.17 \pm 0.66)$ mas yr^{-1}, corresponding to $\mu_S(l, b) \simeq (-5.1, -3.6)$ mas yr^{-1}. This is not unusual in itself, but it was not correct. As indicated by Table 14, the DR3 measurement differs by about 4σ: $\mu_S(E, N) = (-2.40 \pm 0.37, -5.90 \pm 0.30)$ mas yr^{-1}, corresponding to $\mu_S(l, b) \simeq (-6.3, -0.9)$ mas yr^{-1}. We rerun the Bayesian analysis after removing the Gaia measurement of the source proper motion. We find, for the "early-2018 + 2019" Spitzer data set, the following *revised* physical parameters for this event: $M_{host} = 0.076^{+0.069}_{-0.027} M_\odot$, $M_{planet} = 0.21^{+0.19}_{-0.07} M_J$, $D_L = 4.75^{+0.82}_{-1.04}$ kpc, $r_\perp = 1.13^{+0.47}_{-0.25}$ au, $\mu_{hel,rel} = 2.75^{+2.24}_{-0.76}$ mas yr^{-1}, and $P_{bulge} = 0.046$. Hence, the system is somewhat less massive and farther from the Sun than reported by Zang et al. (2022a), although the differences are $<1\sigma$. These should be adopted as the corrected physical parameters for OGLE-2018-BLG-0799.

Thus, taken as a whole, the four events with PPM solutions, high RUWE, and $\Delta\theta < 0''.2$, each show moderate to major independent reasons for concern. Therefore, collectively, they imply that extreme caution should be applied before incorporating Gaia events with high RUWE into the Bayesian analyses of planetary-microlensing events.

Of the remaining six events, the Gaia entries all have low RUWE. For four of these, the Gaia entry is strongly dominated by light from the source, and we review these first.

Gould et al. (2022) incorporated the Gaia proper motion of OGLE-2018-BLG-0932 into their analysis. They noted that its value, $\mu_S(l, b) \simeq (-11.0, +3.8)$ mas yr^{-1}, combined with their own measurement of $\mu_{rel} = 6.2 \pm 0.4$ mas yr^{-1}, strongly favors bulge lenses. As noted by Gould et al. (2022), this event has excellent Spitzer data that will eventually enable a "complete solution," i.e., including both θ_E and π_E.

Jung et al. (2019) combined the Gaia proper-motion measurement for the OGLE-2018-BLG-0596 source with a Spitzer-based π_E measurement to precisely determine the lens mass, distance, and transverse velocity. We note that the subsequent DR3 update did not substantially change this measurement but did substantially reduce its errors.

Kim et al. (2021a) used the Gaia DR2 μ_S measurement in their Bayesian analysis of OGLE-2018-BLG-1428, although they noted the very large error bars. For DR3, the error bars are

reduced by about a factor 2.5, while the central values correspond much more closely to those of a typical bulge star, $\mu_S(l, b) \simeq (-4.4, -3.0)$ mas yr^{-1}. Because they measured $\mu_{rel} = 5.6 \pm 0.4$ mas yr^{-1}, the proper-motion constraints are about equally compatible with either bulge or disk lenses. Hence, the Gaia measurement plays only a small role.

Wang et al. (2022) did not incorporate the Gaia measurement, which corresponds to $\mu_S(l, b) \simeq (-6.5, -4.9)$ mas yr^{-1}, into their Bayesian analysis of OGLE-2018-BLG-0383. Because they measured a relatively slow relative proper motion, $\mu_{rel} = 3.2 \pm 0.3$ mas yr^{-1}, incorporating the Gaia μ_S would have significantly constrained the lens to lie in the bulge. However, because the Einstein radius, $\theta_E = 0.10 \pm 0.01$ mas, was small, the Bayesian analysis already heavily favored bulge lenses. After redoing this analysis with the Gaia constraint, we find that the Bayesian estimates are indeed almost unchanged: the only parameter that changes by more than 0.2σ is the lens distance, $D_L = 7.7 \pm 0.6$ kpc $\rightarrow 7.2 \pm 0.6$ kpc.

For the remaining two events, there was substantial light from another star in addition to that of the source. However, in contrast to the cases of OGLE-2018-BLG-0740 and OGLE-2018-BLG-1269, the Gaia entry was not completely dominated by the lens. Hence, in both cases, the interpretation is fairly complex.

For KMT-2018-BLG-1292, Ryu et al. (2020) estimated that, in the Gaia band, the fraction of total flux due to the source was $\eta = 0.27$, while noting that this number can actually be measured once the individual epochs of Gaia photometry are released. As illustrated in their Figure 7, they were then able to constrain the *direction* of μ_{rel}, which is the same as the direction of π_E, and showed that it was consistent with this direction as determined from the light curve. They argued that this gave confidence to the relatively weak measurement of the *amplitude* of the π_E measurement. They thereby measured the mass and distance of the system with much greater confidence than would be the case without Gaia data. They used DR2, but their results would not have qualitatively changed if DR3 had been available.

OGLE-2018-BLG-0567 is perhaps the most complex case. The key point is that about half the light in the baseline object comes from a blend, whose nature was not investigated by Jung et al. (2021). We find that the source lies just 13 mas from the baseline object, which would seem to virtually rule out that the blend is due to a random field star ($p < 10^{-4}$). Hence, it must be either the lens itself or a companion to the lens or source. The source lies on the lower giant branch, about 1 mag below the red clump (see Figure 6 of Jung et al. 2021), while the blend lies about 0.6 mag redward of this position. Thus, the source and blend are not on the same isochrone, implying that they could only be companions if they were the products of strong binary evolution. However, for these two stars to have interacted, they would have had to have been so close that the blend would have fully participated in the event. Alternatively, they could be part of a 3-body system in which an unseen (or possibly deceased) third body was driven by the Lidov–Kozai mechanism into a tight orbit with the blend star. The blend position is not consistent with being the lens at any distance, given the measurement by Jung et al. (2021) of $\theta_E = 0.21$ mas. The blended light is consistent with being due to an $M \sim 0.2 M_\odot$ M dwarf at $D_L \sim 200$ pc, but if this were a companion to the lens, then the microlens parallax would be $\pi_E = \pi_{rel}/\theta_E \sim 25$, which would have dramatically impacted

the light curve. Moreover, if the blend were this close (regardless of whether it were associated with the lens), then the Gaia parallax would be $\pi \sim 2$ mas, which is not the case. Furthermore, the Gaia proper motion, $\mu_{\mathrm{base}}(l, b) \simeq (-8.9, -0.6)$ mas yr^{-1}, is quite consistent with bulge kinematics. Therefore, despite our initial assessment that an unrelated field star is *virtually ruled out*, this turns out to be a relatively plausible explanation, with the only other possibility being a rare system of a very nearly equal mass binary with a very rare form of 3-body evolution. Hence, the Gaia proper-motion measurement cannot be used to constrain the system.

In summary, among the 32 events, Gaia yielded critically important information for 5, either because the lens dominated the Gaia light (OGLE-2018-BLG-0740, OGLE-2018-BLG-1269, KMT-2018-BLG-1292) or because the Gaia μ_S completed the characterization of lens kinematics for which there was already a *complete solution* that yielded θ_{E} and π_{E} (OGLE-2018-BLG-0596, OGLE-2018-BLG-0932[15]). For two other events (OGLE-2018-BLG-0383, OGLE-2018-BLG-1428), the Gaia measurement tended to corroborate the Bayesian estimates of the lens location. For the remaining 25 events, Gaia did not provide substantial additional information: for 10, there was no Gaia counterpart; for 4, Gaia did not have a PPM solution; 4 had a high RUWE parameter; 5 were corrupted by source confusion; and for 2, Gaia proper motions were not constraining simply because there was no μ_{rel} information from the light curve.

7. Conclusions

We have completed the analysis of the 2018 KMT AnomalyFinder planetary sample by analyzing 9 planetary (or possibly planetary) events from the 84 deg^2 covered by the KMT subprime fields, including 6 that are unambiguously planetary. The principal scientific value of this effort is that it provides the first statistical sample of microlensing planets from KMT and the largest single sample (33 planets from 32 events) that has been published to date. Three of the 6 unambiguous planets were newly discovered by the KMTNet AnomalyFinder, while the other 3 were previously recognized but were not published, presumably because of lack of sufficient interest in them as individual discoveries. Indeed, none of the 6 planets (including, in particular the 3 new AnomalyFinder planets) is of great individual interest. For example, they lie in fairly typical regimes of parameter space. However, the fact that none of these planets is individually notable is itself quite interesting because, of the 8 new AnomalyFinder planets in the prime fields (Hwang et al. 2022; Wang et al. 2022; Gould et al. 2022), 2 (OGLE-2018-BLG-0506 and OGLE-2018-BLG-0977) have mass ratios $q < 10^{-4}$, while a third is at an unusually wide separation, $s = 2.45$ (OGLE-2018-BLG-0383).

This is one of several facts that led us to a systematic 6D study ($\log q$; $I_{\mathrm{anom}} \equiv I_s - 2.5 \log[A(u_{\mathrm{anom}})]$; AnomalyFinder versus by-eye; caustic versus noncaustic; major-image versus minor-image perturbation; and prime versus subprime KMT fields) of the entire sample of 33 planets in Section 6.2. Many interesting patterns emerged, the two most striking of which are the apparent floor on planetary detections $I_{\mathrm{anom}} < 18.75$ and the

dearth of by-eye discoveries of non-caustic-crossing anomalies for $\log q < -3$.

The opportunity presented by this large, homogeneously selected planet sample also led us to the first systematic investigation (in Section 6.3) of the role of Gaia in the analysis of planetary-microlensing events. We found that of the 32 planetary events, Gaia played a major role in the characterization of 5 and a modest role in the characterization of another 2. One important conclusion that came out of this systematic investigation that was not obvious from the previous event-by-event approach is that the Gaia proper-motion measurement should not have been incorporated into the Bayesian analysis of OGLE-2018-BLG-0799. In Section 6.3, we have presented *revised* physical parameters for this event based on Bayesian analysis that excludes the Gaia measurement.

ORCID iDs

Youn Kil Jung https://orcid.org/0000-0002-0314-6000
Weicheng Zang https://orcid.org/0000-0001-6000-3463
Cheongho Han https://orcid.org/0000-0002-2641-9964
Andrzej Udalski https://orcid.org/0000-0001-5207-5619
Michael D. Albrow https://orcid.org/0000-0003-3316-4012
Sun-Ju Chung https://orcid.org/0000-0001-6285-4528
Kyu-Ha Hwang https://orcid.org/0000-0002-9241-4117
Yoon-Hyun Ryu https://orcid.org/0000-0001-9823-2907
In-Gu Shin https://orcid.org/0000-0002-4355-9838
Yossi Shvartzvald https://orcid.org/0000-0003-1525-5041
Hongjing Yang https://orcid.org/0000-0003-0626-8465
Jennifer C. Yee https://orcid.org/0000-0001-9481-7123
Seung-Lee Kim https://orcid.org/0000-0003-0562-5643
Chung-Uk Lee https://orcid.org/0000-0003-0043-3925
Byeong-Gon Park https://orcid.org/0000-0002-6982-7722
Richard W. Pogge https://orcid.org/0000-0003-1435-3053
Michał K. Szymański https://orcid.org/0000-0002-0548-8995
Jan Skowron https://orcid.org/0000-0002-2335-1730
Igor Soszyński https://orcid.org/0000-0002-7777-0842
Paweł Pietrukowicz https://orcid.org/0000-0002-2339-5899
Szymon Kozłowski https://orcid.org/0000-0003-4084-880X
Krzysztof Ulaczyk https://orcid.org/0000-0001-6364-408X
Patryk Iwanek https://orcid.org/0000-0002-6212-7221
Marcin Wrona https://orcid.org/0000-0002-3051-274X

References

Alard, C., & Lupton, R. H. 1998, ApJ, 503, 325
Albrow, M. D. 2017, Michaeldalbrow/Pydia: InitialRelease On Github, vv1.0.0, Zenodo, doi:10.5281/zenodo.268049

---

[15] Strictly speaking, this *will* be true of OGLE-2018-BLG-0932 once the Spitzer data are analyzed.

Albrow, M. D., Horne, K., Bramich, D. M., et al. 2009, MNRAS, 397, 2099
Bensby, T., Yee, J. C., Feltzing, S., et al. 2013, A&A, 549, A147
Bessell, M. S., & Brett, J. M. 1988, PASP, 100, 1134
Gaia Collaboration, Brown, A. G. A., Vallenari, A., et al. 2018, A&A, 616, A1
Gaia Collaboration, Prusti, T., de Bruijne, J. H. J., et al. 2016, A&A, 595, A1
Gaudi, B. S. 1998, ApJ, 506, 533
Gaudi, B. S., & Gould, A. 1997, ApJ, 486, 85
Gonzalez, O. A., Rejkuba, M., Zoccali, M., et al. 2012, A&A, 543, A13
Gould, A., Dong, S., Gaudi, B. S., et al. 2010, ApJ, 720, 1073
Gould, A., Han, C., & Zang, W. 2022, A&A, 664A, 13
Gould, A., Ryu, Y.-H., Calchi Novati, S., et al. 2020, JKAS, 53, 9
Gould, A., Zang, W., Mao, S., & Dong, S. 2021, RAA, 21, 133
Griest, K., & Safizadeh, N. 1998, ApJ, 500, 37
Han, C., Albrow, M. D., Chung, S.-J., et al. 2021b, A&A, 652, 145
Han, C., Gould, A., Albrow, M. D., et al. 2021c, A&A, 658A, 62
Han, C., Udalski, A., Gould, A., et al. 2016, ApJ, 828, 53
Han, C., Udalski, A., Kim, D., et al. 2021a, A&A, 650A, 89
Han, C., Yee, J. C., Udalski, A., et al. 2019, AJ, 158, 102
Henderson, C. B., Gaudi, B. S., Han, C., et al. 2014, ApJ, 794, 52
Hog, E., Novikov, I. D., & Polanarev, A. G. 1995, A&A, 294, 287
Hwang, K.-H., Zang, W., Gould, A., et al. 2022, AJ, 163, 43
Jung, Y. K., Han, C., Udalski, A., et al. 2021, AJ, 161, 293
Jung, Y. K., Gould, A., Udalski, A., et al. 2019, AJ, 158, 28
Jung, Y. K., Gould, A., Udalski, A., et al. 2020a, AJ, 160, 148
Kervella, P., Bersier, D., Mourard, D., et al. 2004a, A&A, 428, 587
Kervella, P., Thévenin, F., Di Folco, E., & Ségransan, D. 2004b, A&A, 426, 297
Kim, D.-J., Kim, H.-W., Hwang, K.-H., et al. 2018a, AJ, 155, 76
Kim, H.-W., Hwang, K.-H., Kim, D.-J., et al. 2018b, arXiv:1804.03352
Kim, S.-L., Lee, C.-U., Park, B.-G., et al. 2016, JKAS, 49, 37
Kim, H.-W., Hwang, K.-H., Shvartzvald, Y., et al. 2018c, arXiv:1806.07545
Kim, Y.-H., Chung, S.-J., Udalski, A., et al. 2021a, MNRAS, 503, 2706
Kim, Y. H., Chung, S.-J., Yee, J.-C., et al. 2021b, AJ, 162, 17
Kondo, I., Yee, J. C., Bennett, D. P., et al. 2021, AJ, 162, 77
Kubiak, M., & Szymański, M. K. 1997, AcAau, 47, 319
Minniti, D., Lucas, P. W., Emerson, J. P., et al. 2010, NewA, 15, 433
Minniti, D., Lucas, P., & Team, V. V. V. 2017, yCAT, 2348, 0
Miyamoto, M., & Yoshii, Y. 1995, AJ, 110, 1427
Nataf, D. M., Gould, A., Fouqué, P., et al. 2013, ApJ, 769, 88
Paczyński, B. 1986, ApJ, 304, 1
Park, B.-G., DePoy, D. L., Gaudi, B. S., et al. 2004, ApJ, 609, 166
Rybizki, J., Green, G. M., Rix, H.-W., et al. 2022, MNRAS, 510, 2597
Ryu, Y.-H., Hwang, K.-H., Gould, A., et al. 2019, AJ, 158, 151
Ryu, Y.-H., Hwang, K.-H., Gould, A., et al. 2021, AJ, 162, 96
Ryu, Y.-H., Jung, Y. K., Yang, H., et al. 2022, AJ, 164, 180
Ryu, Y.-H., Navarro, M. G., Gould, A., et al. 2020, AJ, 159, 58
Schechter, P. L., Mateo, M., & Saha, A. 1993, PASP, 105, 1342
Schlafly, E. F., Green, G. M., Lang, D., et al. 2018, ApJS, 234, 39
Shvartzvald, Y., Maoz, D., Udalski, A., et al. 2016, MNRAS, 457, 4089
Suzuki, D., Bennett, D. P., Sumi, T., et al. 2016, ApJ, 833, 145
Szymański, M. K. 2005, AcAau, 55, 43
Szymański, M. K., Udalski, A., Soszyński, I., et al. 2011, AcAau, 61, 83
Tomaney, A. B., & Crotts, A. P. S. 1996, AJ, 112, 2872
Udalski, A. 2003, AcAau, 53, 291
Udalski, A., Szymanski, M., Kaluzny, J., et al. 1994, AcAau, 44, 227
Udalski, A., Szymański, M., Kubiak, M., et al. 2002, AcAau, 52, 217
Walker, M. A. 1995, ApJ, 453, 37
Wang, H., Zang, W., Zhu, W., et al. 2022, MNRAS, 510, 1778
Woźniak, P. R. 2000, AcAau, 50, 421
Yee, J. C., Gould, A., & Beichman, C. 2015, ApJ, 810, 155
Yee, J. C., Zang, W., Udalski, A., et al. 2021, AJ, 162, 180
Yoo, J., DePoy, D. L., Gal-Yam, A., et al. 2004, ApJ, 603, 139
Zang, W., Hwang, K.-H., Udalski, A., et al. 2021, AJ, 162, 163
Zang, W., Shvartzvald, Y., Udalski, A., et al. 2022a, MNRAS, 514, 5992
Zang, W., Yang, H., Han, C., et al. 2022b, MNRAS, 515, 928
Zhang, K., & Gaudi, B. S. 2022, ApJL, 936, L22
Zhu, W., Penny, M., Mao, S., Gould, A., & Gendron, R. 2014, ApJ, 788, 73